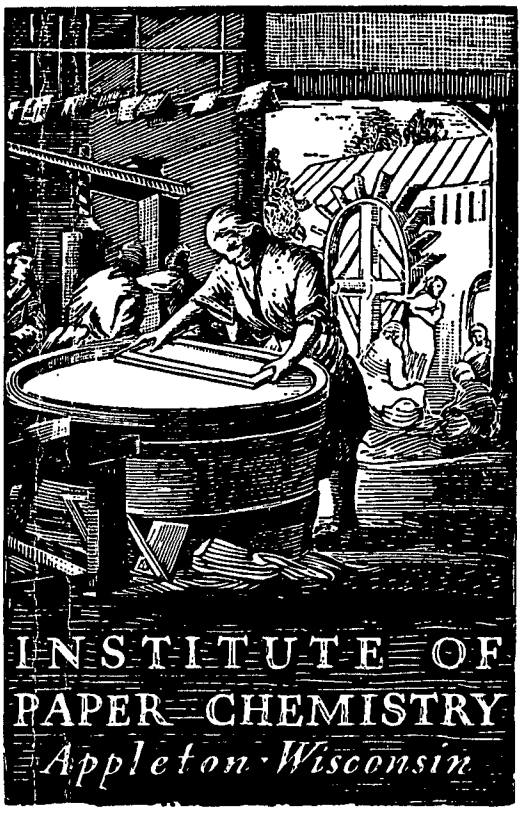

HIGHER-CONSISTENCY PROCESSING

Project 3479

Report Two
A Progress Report
to
MEMBERS OF THE INSTITUTE OF PAPER CHEMISTRY

September 20, 1983

THE INSTITUTE OF PAPER CHEMISTRY

Appleton, Wisconsin

HIGHER-CONSISTENCY PROCESSING

Project 3479

Report Two

A Progress Report

to

MEMBERS OF THE INSTITUTE OF PAPER CHEMISTRY

September 20, 1983

TABLE OF CONTENTS

THE INSTITUTE OF PAPER CHEMISTRY

Appleton, Wisconsin

HIGHER-CONSISTENCY PROCESSING

SUMMARY

The ability to form a sheet of paper with good mechanical properties from a concentrated suspension of fibers could lead to smaller processing equipment, shorter wire sections, reduced processing energy consumption, and more controllable paper property development. To achieve proper high-consistency forming, however, it is necessary to disrupt the fiber flocs typical of such suspensions for a period of time sufficient to properly orient the fibers and form the sheet. Hence an understanding of the hydrodynamics of floc disruption, reflocculation, and fiber alignment is critical to the successful design of forming and other processing equipment for fiber suspensions with unusually high concentrations. The objective of this project is to generate the necessary fundamental information.

A flow channel with a converging-diverging section was used to generate turbulence for floc disruption and allow subsequent reflocculation. Fiber optic probes were used to provide a direct indication of floc-size distributions at various points along the flow channel. Pressure fluctuation measurements were used to complement and corroborate the fiber optic probe data. Power spectral density analysis of the signals from given probes was used to characterize the floc size distribution at a given station. Coherence function relationships between the signals from selected pairs of probes were used to estimate the build-up or decay of flocs of a given size over the region between the probes.

Experimental studies were conducted for fiber weight concentrations of 1 and 2% - high compared to normal forming consistencies - and flow velocities from 1500-2000 fpm (7.6-10.2m/s).

Additionally, the motion of a labeled fiber in a concentrated suspension, undergoing simple shear or simple elongational flow, was modeled to estimate the time evolving shape and orientation of the fiber.

The following summarizes the essential findings from the various analyses and experiments:

1. At low velocities, the turbulence levels were not sufficient to disrupt the large flocs. Some smaller flocs or fibers interact to form larger ones.
2. At high velocities, all flocs were disrupted, and flocs of single fiber size were stable immediately downstream of the turbulence generators. Their relative number eventually decreased as larger flocs were formed. The distance (times) over which they remained stable increased with fiber concentration.
3. After break-up, the flocs attained a new steady-state size distribution at some point downstream of the turbulence generators. The distance required increased with average flow velocity and fiber concentration.
4. For a given velocity the larger flocs were disrupted more effectively, particularly at the higher concentrations. Increasing fiber concentration promoted the reflocculation process under some conditions and impeded it under others.
5. The intensity of the pressure fluctuations was consistent with the flocculation measurements and established the state of fluidization of the suspension. Such measurements may prove effective in extending the experiments to concentrations beyond the useful range of the fiber optic probes.
6. The model of Goddard and Huang (17), for motion of a slender thread in a concentrated suspension, has been used to examine the effect of flow field and initial conditions on the evolution in time of fiber shape and alignment in the direction of flow. This study shows that fibers in concentrated suspensions may be aligned only in elongational flows. Furthermore, the time required for alignment is

independent of initial shape and orientation, an important result from the standpoint of designing new devices for forming paper from concentrated wood fiber suspensions.

INTRODUCTION

During the forming of a sheet of paper, good dispersion of the individual fibers is necessary to insure good mechanical properties of the product. However, wood fibers in a suspension undergoing deformation have an inherent tendency to interact with each other and form aggregates (flocs) due to mechanical entanglement (1). Thus, prior to dispersing the fibers, the flocs must be effectively disrupted. Because this process is facilitated at lower fiber concentrations, paper is usually formed from dilute suspensions. Papermaking under these conditions requires handling large amounts of water, which in turn, results in excessive size of the equipment.

One approach for reducing the size of papermaking equipment and possibly its operating costs is to form paper from a concentrated suspension, known in the paper industry as "high-consistency forming" (2,3). Several studies have examined the feasibility of such an approach. Currently, high-consistency pilot formers perform two operations: (1) generation of turbulence levels sufficient to break up the fiber flocs and disperse the fibers and (2) formation of a homogeneous fiber network as the turbulence decays (4). Their use potentially eliminates the need for the wire section of paper machines used to drain water from the web and consolidate the sheet of paper (5). The web leaving these high-consistency formers typically contains the same percentage of fibers by weight as that leaving the wire section in conventional paper machines.

Paper formed from concentrated suspensions tends to have a more felted structure than its counterpart formed from dilute ones. This felted structure has a high porosity which facilitates water removal from the web; also, it is considered the main contributing factor to the poor tensile strength of the paper; compressive strength may actually be acceptable. Fundamental to improving tensile strength

is the ability to align the fibers prior to the formation of the fiber network to produce a sheet of paper with a layered structure similar to that obtained from dilute suspensions. Fiber alignment requires breakup of the flocs, followed by maintenance of a floc-free state for the necessary period of time.

Floc breakup and formation are competing effects that are both promoted by turbulence (3). However, studies of turbulent flow of fiber suspensions (6) have demonstrated that even at low concentrations the presence of the fibers attenuates the turbulence. This effect is accentuated with increasing fiber concentration. Furthermore, there is some experimental and theoretical evidence that the mobility of fibers relative to their suspending medium is hindered as concentration increases (7,8). Thus, it seems possible, that while intuitively it is expected that an increase in fiber concentration promotes flocculation, under given sets of conditions the effect may be the opposite. It was the purpose of this study to examine the effects of average flow velocity and fiber concentration on the breakup of flocs through a turbulence generator and the reflocculation process in the downstream section for relatively concentrated suspensions. Studies reported in the literature have dealt only with dilute suspensions (9). A second purpose was to predict the time required to align a fiber in a concentrated suspension as a function of its initial shape in different types of flow fields.

EXPERIMENTAL EQUIPMENT

The experiments were performed in the flow system depicted in Fig. 1. It consists of a flow channel of rectangular cross section (0.1524 m x 0.0127 m), a storage tank with a mixer for the fiber suspension, a centrifugal pump, a magnetic flowmeter, and a recirculation loop. The fibers were continuously recirculated for the duration of an experiment with an average residence time in the storage tank of about 60 seconds. Approximately 1.5 m downstream of the inlet to the channel is a converging/diverging section shown in Fig. 2 (not drawn to scale) used as a turbulence generator. This particular design was chosen because it resembles typical pilot devices used in paper forming from concentrated suspensions. At the constriction (separation = 0.005 m) the average flow velocity was 2.5 times higher than in the upstream section of the channel. The turbulent wake generated at this point caused the breakup of flocs. Also shown in Fig. 2 are the locations of the fiber optic probes and pressure transducers used to measure the state of flocculation of the suspension and pressure fluctuations, respectively. The fiber optic probes covered a distance up to 0.13 m downstream of the trailing edge of the diverging section, and the locations of the pressure transducers extended to 0.15 m.

The y-shaped fiber optic probes (shown in Fig. 3) used in this study were similar to those previously used for flocculation measurements in fiber suspensions (10,11). Each probe consists of two separate bundles of light guides coming together at one end. One was used to carry light from a source to the common end which was mounted flush with the bottom plate of the channel. The light was transmitted into the suspension, and the fraction reflected by the passing flocs was carried by the other bundle of light guides to a photodiode which converted the fluctuating light into a fluctuating analog signal.

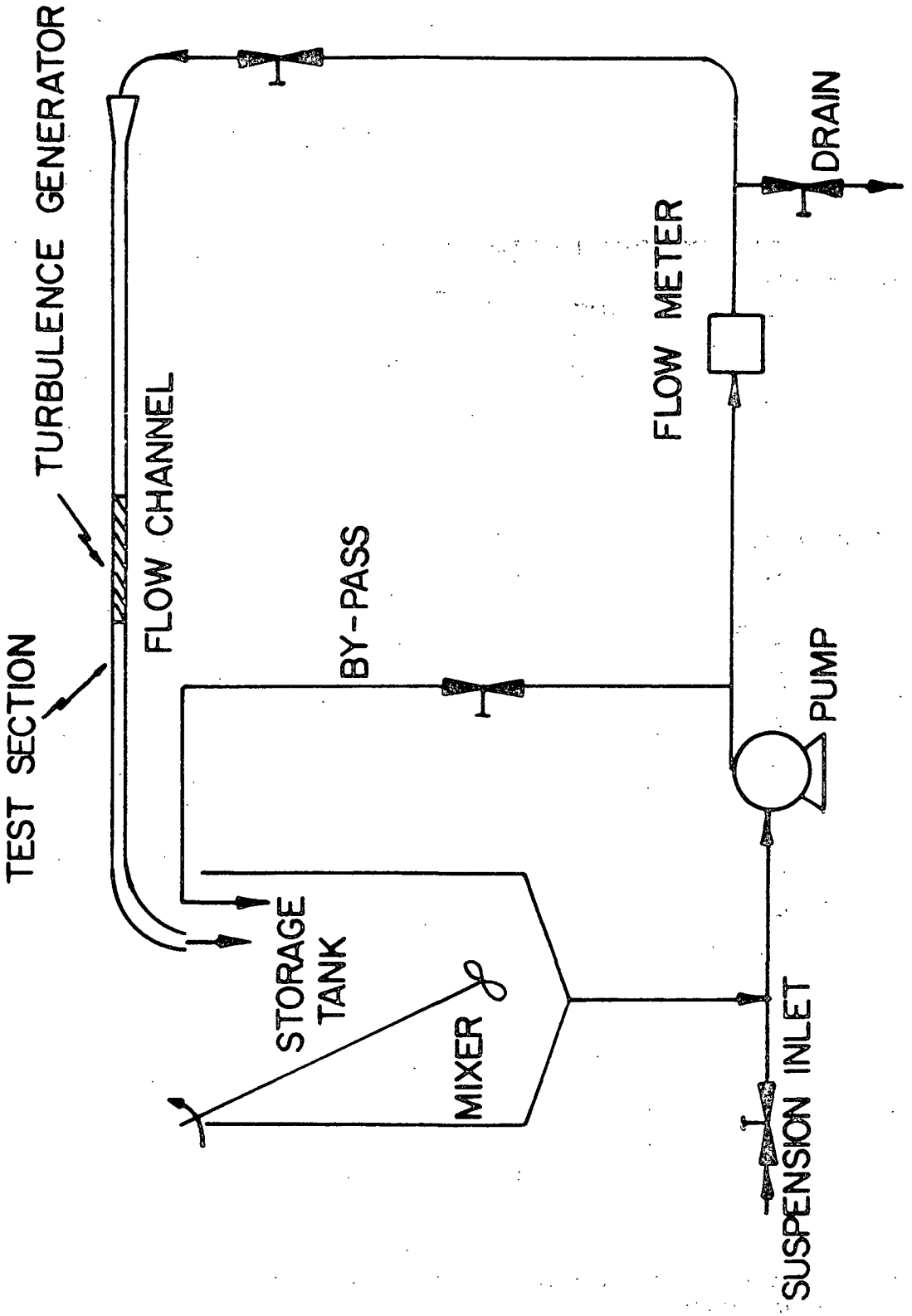

Figure 1. Schematic of flow system.

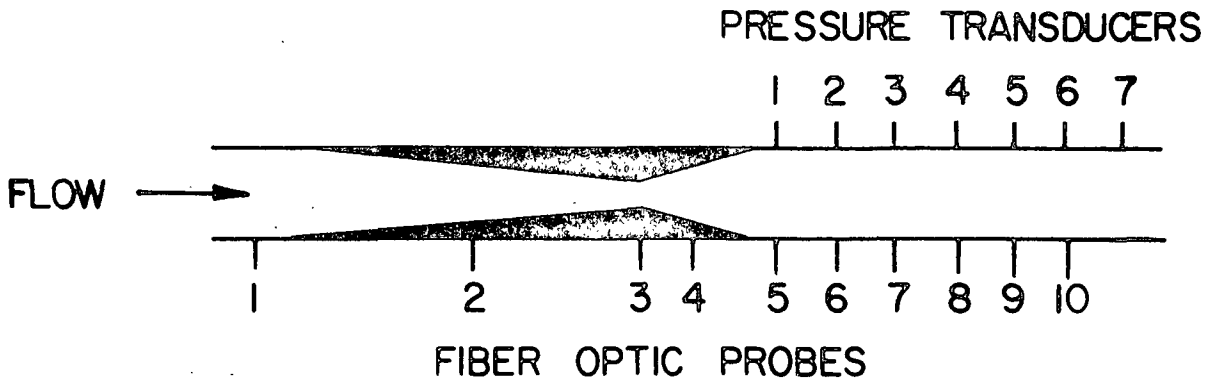

FIBER OPTIC PROBE	PRESSURE TRANSDUCER	DISTANCE FROM TURBULENCE GENERATOR (mm)
5	1	7.94
6	2	31.75
7	3	55.56
8	4	79.37
9	5	103.19
10	6	127.00
	7	150.00

Figure 2. Schematic of converging/diverging section used as turbulence generator and location of fiber optic probes and pressure transducers.

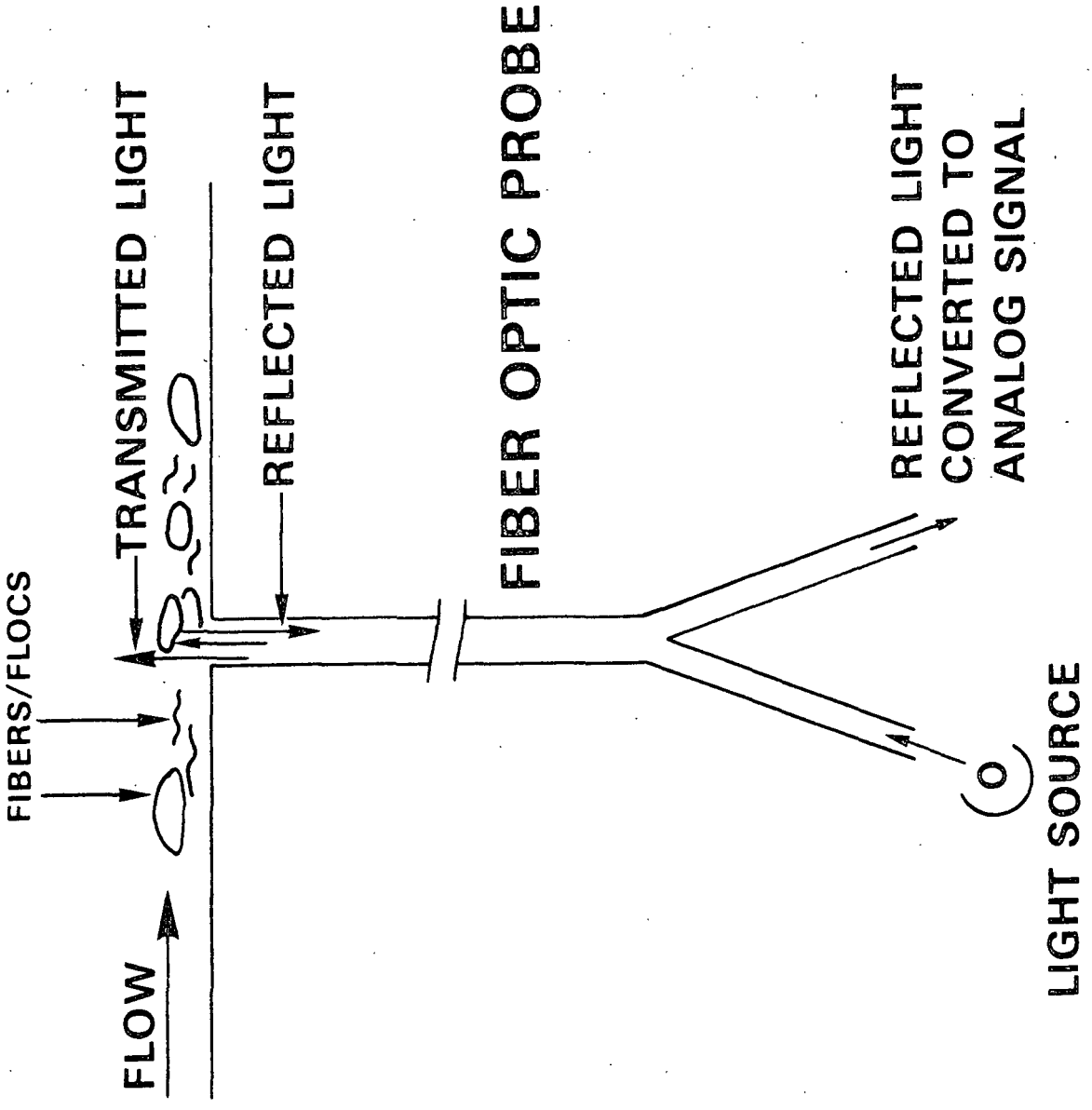

Figure 3. Schematic of fiber optic probe.

The analog signal was sampled using a Tracor Northern 1710 data acquisition unit equipped with a Fast Fourier Transform (FFT) module. The sampling frequency was varied according to the flow velocity; values as high as 100 kHz were used. Power spectral density functions (PSD) were calculated from the sampled signals using the FFT module. The PSD as a function of frequency at a given velocity represents the size distribution of flocs in the suspension, because the intermittency of the reflected light depends on floc size.

The flocculation measurements were complemented with the measurement of the intensity of pressure fluctuations at the wall of the channel using pressure transducers to determine the relative state of fluidization of the suspension. This same technique has been previously used for similar measurements in solid/gas systems (12,13).

RESULTS FROM PSD ANALYSIS

The fibers used in this study were softwood bleached kraft pulp fibers with the length distribution shown in Fig. 4. The majority of the fibers had lengths in the range from 0.5-2.0 mm. The arithmetic and weighted average fiber lengths were 1.9 and 2.6 mm, respectively. The concentration of fibers in suspension was expressed as percent by weight of ovendry fibers, i.e.,

$$C(\%) = \left[\frac{\text{weight of ovendry fibers}}{\text{weight of ovendry fibers + weight of water}} \right] \times 100\% \qquad (1)$$

This convention is used throughout the pulp and paper industry, and we have adopted it here. From a hydrodynamics viewpoint, it is the volume concentration of the fibers in suspension that is important. However, because of the hygroscopic nature of cellulose, wood fibers in a wet state absorb water, and the determination of the amount absorbed is rather tedious and difficult. Since we used fibers of only one type, it is reasonable to express their concentration in the manner discussed above.

The amount of light reflected by the fibers in suspension, in principle, should increase linearly with concentration. At high concentrations, complex light scattering effects become a dominant factor, and the relation of reflected light to concentration ceases to be linear. It is essential to determine the concentration at which nonlinear effects set in because it establishes the maximum concentration for which the fiber optic probes are suitable. Figure 5 is a plot of the intensity of reflected light expressed in millivolts as a function of fiber concentration for fiber optic probe 1 at an average velocity of 10.2 m/s. Up to C = 3%, the response with increasing concentration is linear within 4%. Beyond this concentration, nonlinear effects become important. Other probes behave similarly at this and other

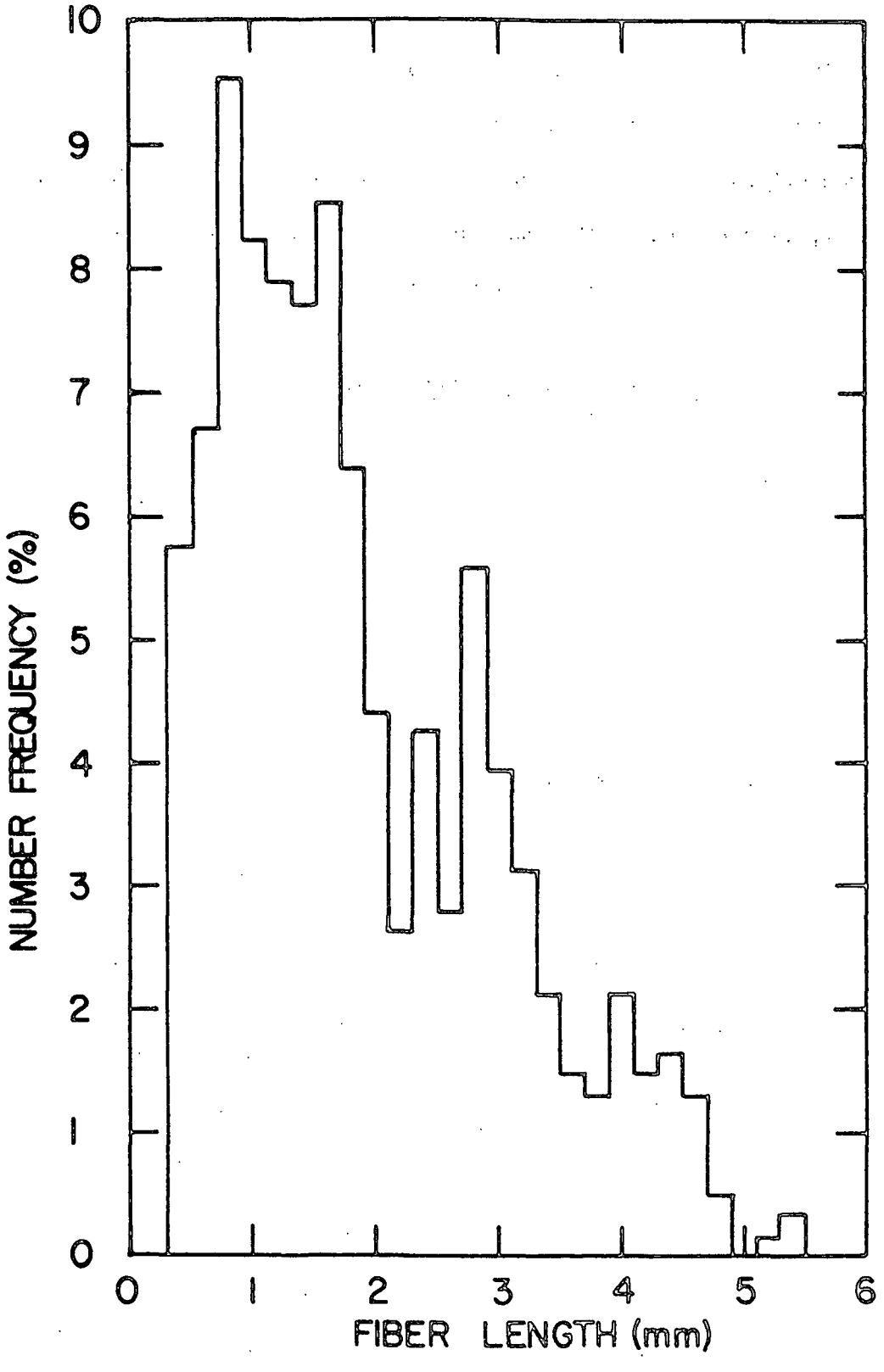

Figure 4. Length distribution of fibers.

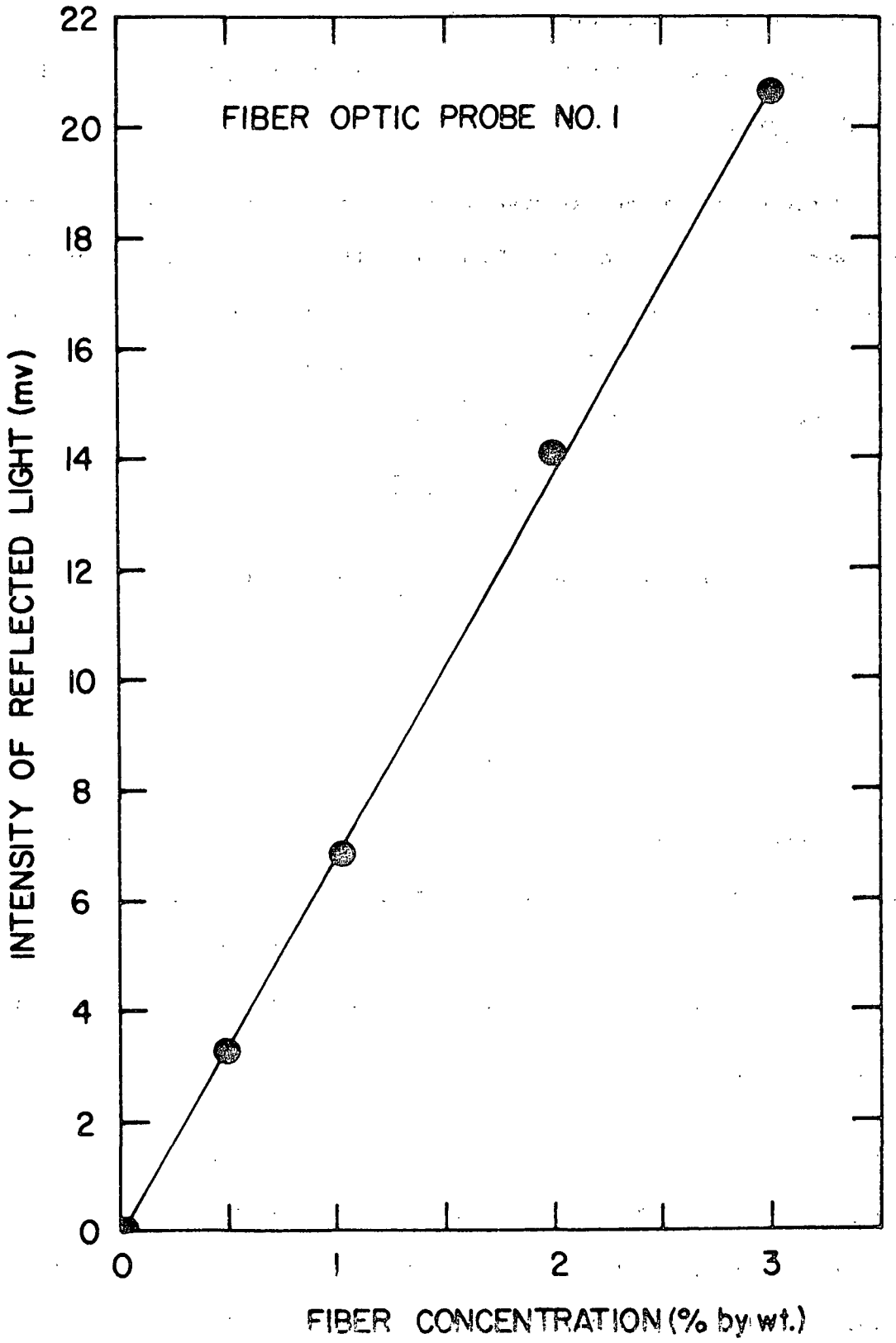

Figure 5. Intensity of reflected light vs. fiber concentration for fiber optic probe 1 at $\overline{u}$ = 10.2 m/s.

velocities. We limit the results discussed below to C = 1% and 2%. These fiber concentrations, although not considered high with respect to other papermaking operations, are nevertheless higher than those from which paper is conventionally formed (C < 1%, typically ~ 0.5%).

The differences in the calibration curves of the different photodiodes and light guides were built into the PSD. To compare the floc size distribution curves at different locations in the test section, the PSD's were normalized with the r.m.s. value of reflected light for the corresponding probe to obtain a relative power spectral density function (RPSD) given by

$$RPSD = PSD/\overline{c'^2} \tag{2}$$

Futhermore, the RPSD's were converted from a frequency to a wavelength domain using the expressions

$$\ell = \bar{u}/f \tag{3}$$

and

$$RPSD(\ell) = (f^2/\bar{u})\ RPSD(f) \tag{4}$$

Thus, RPSD(ℓ) represents the relative occurrence of flocs of different sizes ℓ. Data were taken at all probe locations shown in Fig. 2. However, we present here only the results for probes 1, 5, 7, and 10 because they provide an adequate picture of the change in flocculation across the turbulence generator and the process downstream.

EFFECT OF AVERAGE FLOW VELOCITY

Figures 6, 7, and 8 are plots of RPSD vs. ℓ for a suspension with fiber concentration C = 1% at $\bar{u}$ = 7.6, 9.1, and 10.2 m/s, respectively. The curves are marked 1, 5, 7, and 10 to denote the size distribution at the locations of probes 1, 5, 7, and 10, respectively. At $\bar{u}$ = 7.6 m/s, the curves in Fig. 6 indicate that, as

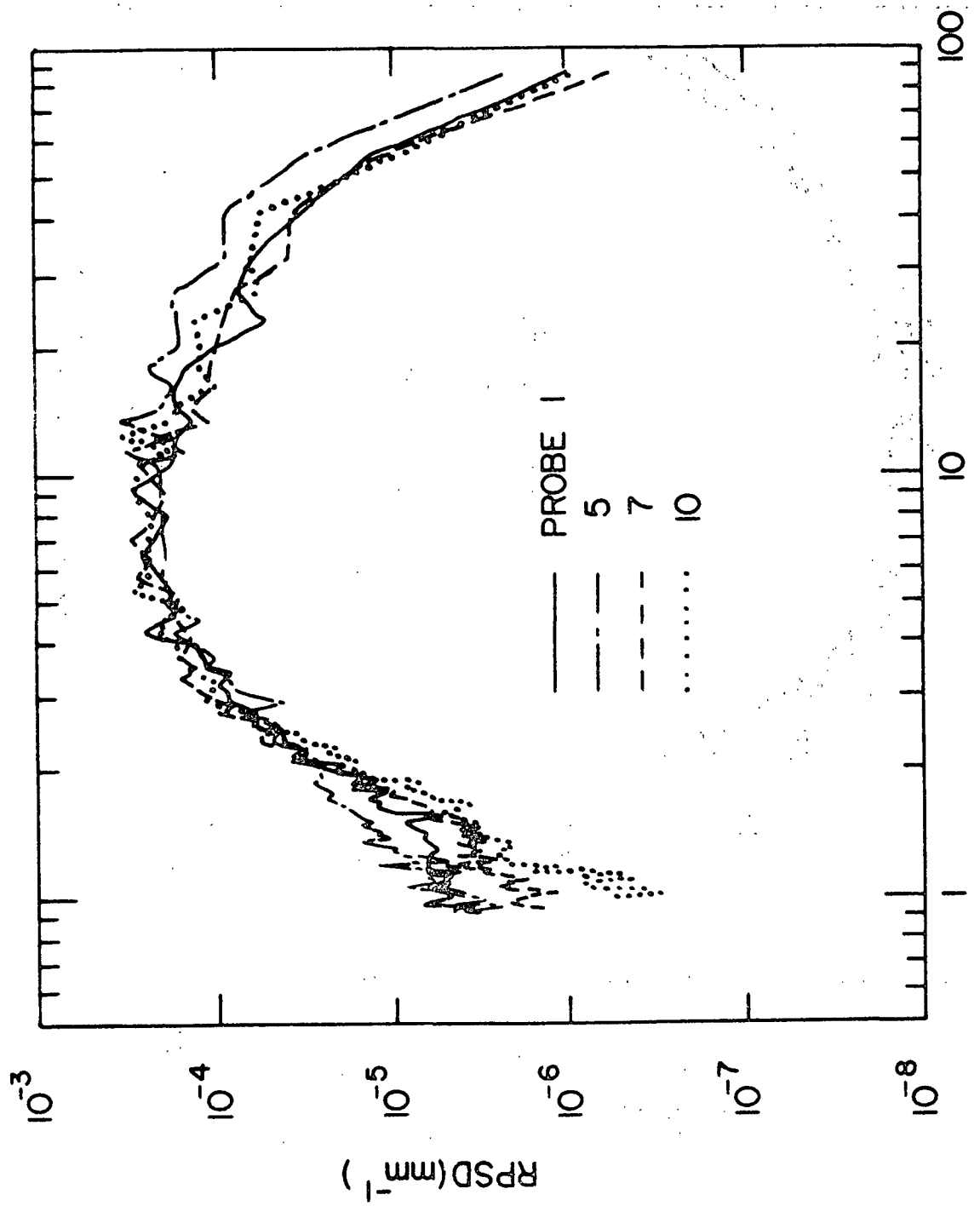

Figure 6. RPSD curves for C = 1% at $\bar{u}$ = 7.6 m/s.

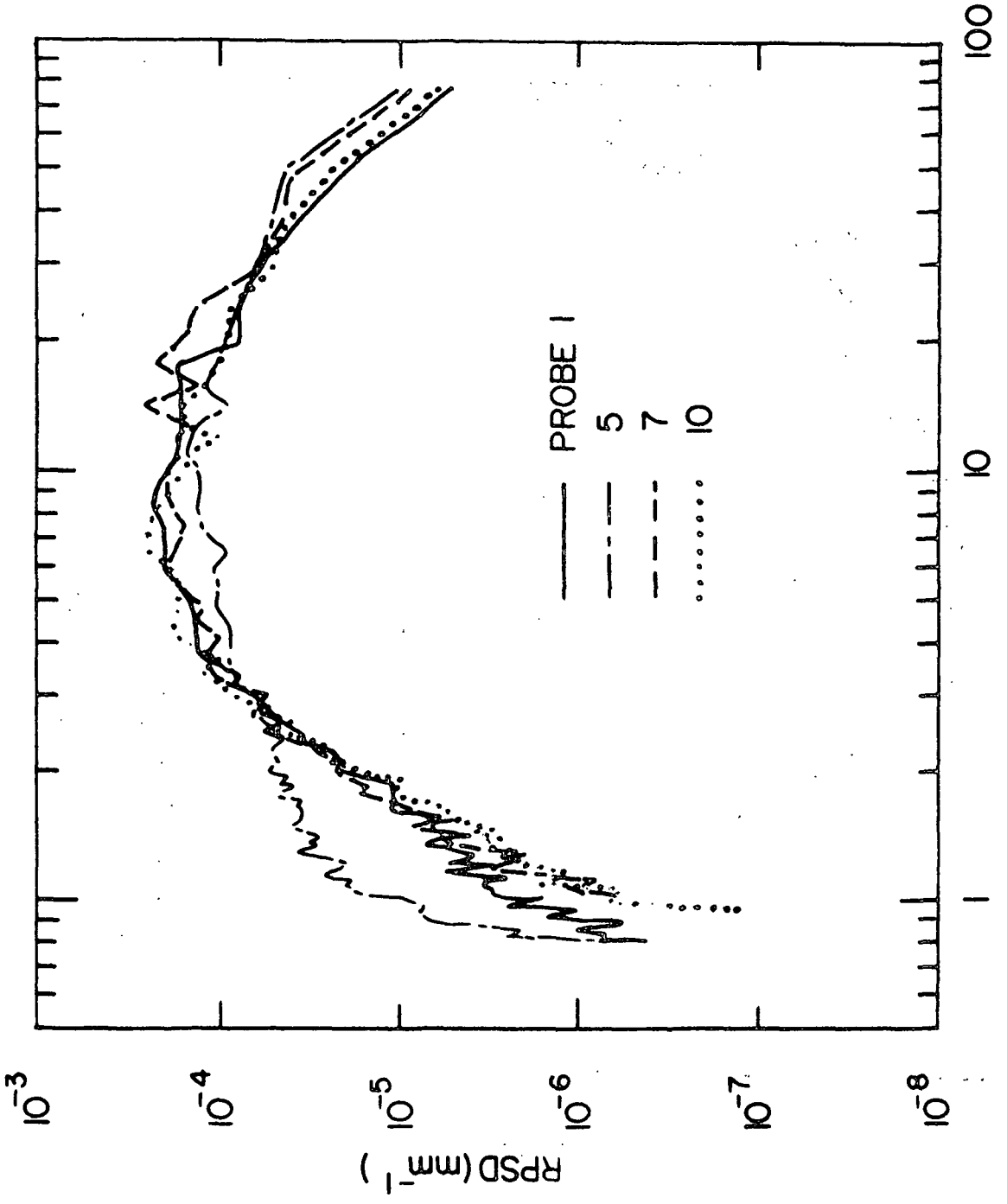

Figure 7. RPSD curves for C = 1% at $\bar{u}$ = 9.1 m/s.

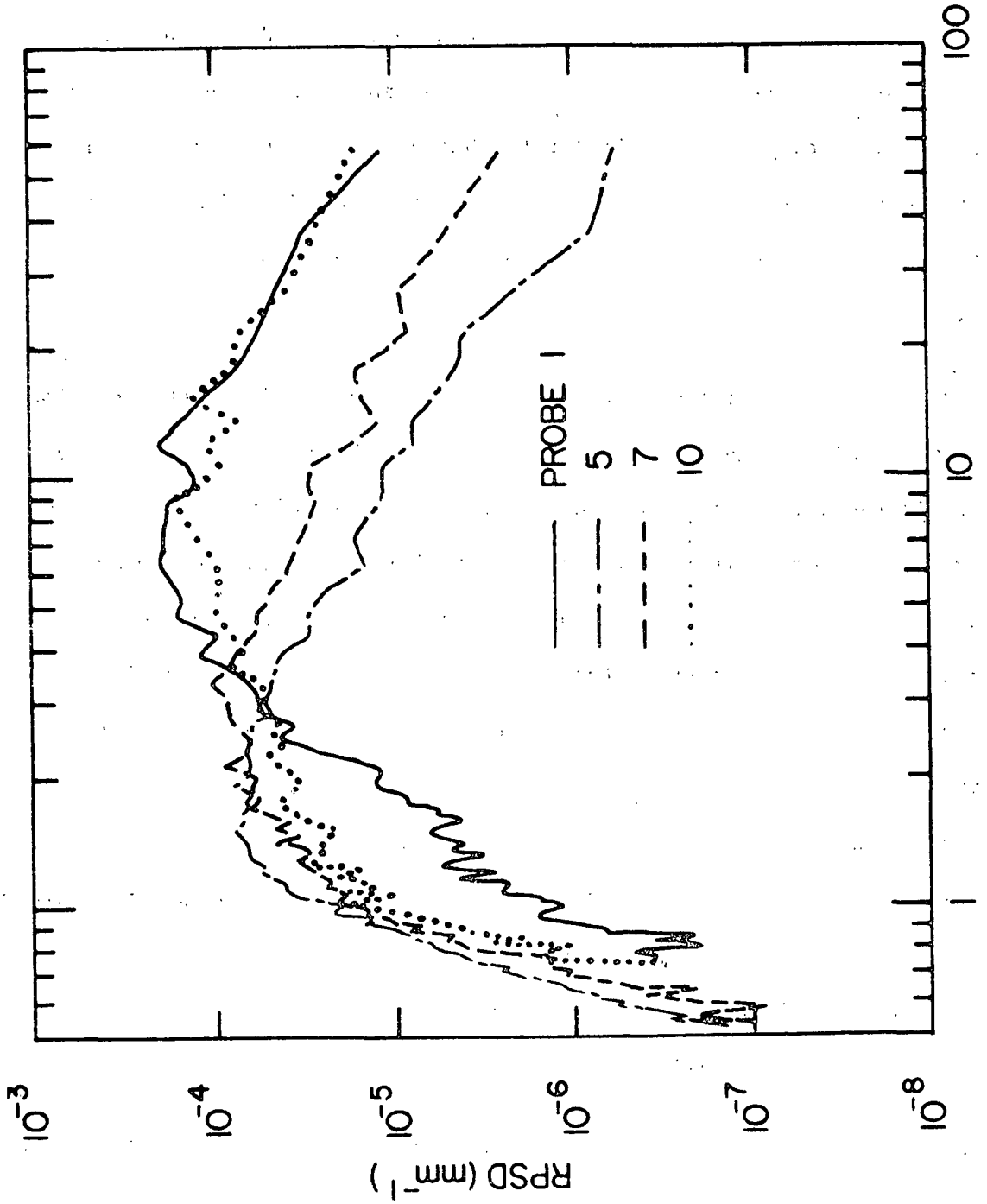

Figure 8. RPSD curves for C = 1% at $\bar{u}$ = 10.2 m/s.

the suspension flowed through the converging/diverging channel, the number of flocs in the approximate range $2.4 < \ell < 9$ mm experienced a slight net reduction, while those corresponding to $1.5 < \ell < 2.4$ mm and $\ell > 10$ mm increased. Downstream of the turbulence generator the fraction of both the larger and small flocs decreased, and the size distribution curve became similar to that upstream (curve 1). It is also noticed that the size distribution curves 7 and 10 are not significantly different, an indication that the flocs may have attained a steady-state size distribution between locations 5 and 7.

Increasing the velocity to 9.1 m/s (Fig. 7) resulted in a net reduction of flocs over a wider size range than at 7.6 m/s, $3 \leq \ell \leq 20$ mm. The larger stresses generated within the turbulence generator at the higher velocities were able to disrupt larger flocs more effectively. Still, at this velocity, the numbers of the largest and smallest flocs both increased across the turbulence generator. The increase in the relative fraction of the latter, however, was considerably higher than at 7.6 m/s. Downstream of the turbulence generator, due to the higher velocity, the mobility of the fibers was higher, and the reflocculation process occurred at a faster rate than at 7.6 m/s. In contrast to the previous case, at this velocity the larger flocs did not reach a steady-state size distribution prior to probe 7. The increase in the number of large flocs observed here as the suspension flowed through the converging/diverging section was also observed by Duffy and Norman (14) for flow through a constriction.

The disruption of flocs at $\bar{u} = 10.2$ m/s (Fig. 8) was significantly higher compared to that at the lower velocities discussed above. The maximum in the size distribution curve shifted from 5-9 mm upstream (curve 1) to close to 1.5 mm immediately downstream (curve 5) of the turbulence generator. The largest flocs were

practically all disrupted. Because of the higher velocity, the reflocculation process took place at a much faster rate than before, and the number of large flocs eventually increased and reached a value comparable to that in the upstream distribution (curve 1). Still, a considerable number of small flocs or fibers existed at the location of probe 10. The net depletion occurred for the intermediate size flocs. As the turbulence decayed, the relative fiber motion possibly also decayed, and large flocs in the form of a continuous network were formed.

The amplitude of the pressure fluctuations measured with the pressure transducers, $(\sqrt{\overline{p'^2}})$, is plotted as a function of position downstream of the turbulence generator (Fig. 9). At $\bar{u}$ = 7.6 and 9.1 m/s as a result of the existence of more of the larger flocs as shown by floc-size distribution curve 5 in Fig. 6 and 7, the pressure fluctuations were more intense. As the suspension attained a steady-state size distribution which was accompanied by the disappearance of the larger flocs, the intensity of the pressure fluctuations decreased. As the large flocs disappeared downstream of the turbulence generator at $\bar{u}$ = 7.6 m/s, the pressure fluctuations decreased and reached a constant value at 80 mm, since the suspension attained a steady-state size distribution. At $\bar{u}$ = 9.1 m/s, the pressure fluctuations experienced a sharper decrease due to the disappearance of the larger flocs and the presence of a significant number of the smaller ones. At $\bar{u}$ = 10.2 m/s, consistent with the large number of small flocs (possibly fibers) present immediately downstream of the turbulence generator, the intensity of the pressure fluctuations was low and fairly constant up to a distance of 0.1 m; beyond this position it increases. Size distribution curve 10 (Fig. 8), which corresponds to a distance of 0.127 m, shows an increase in the relative number of the larger flocs, which causes the increase in the intensity of the pressure fluctuations.

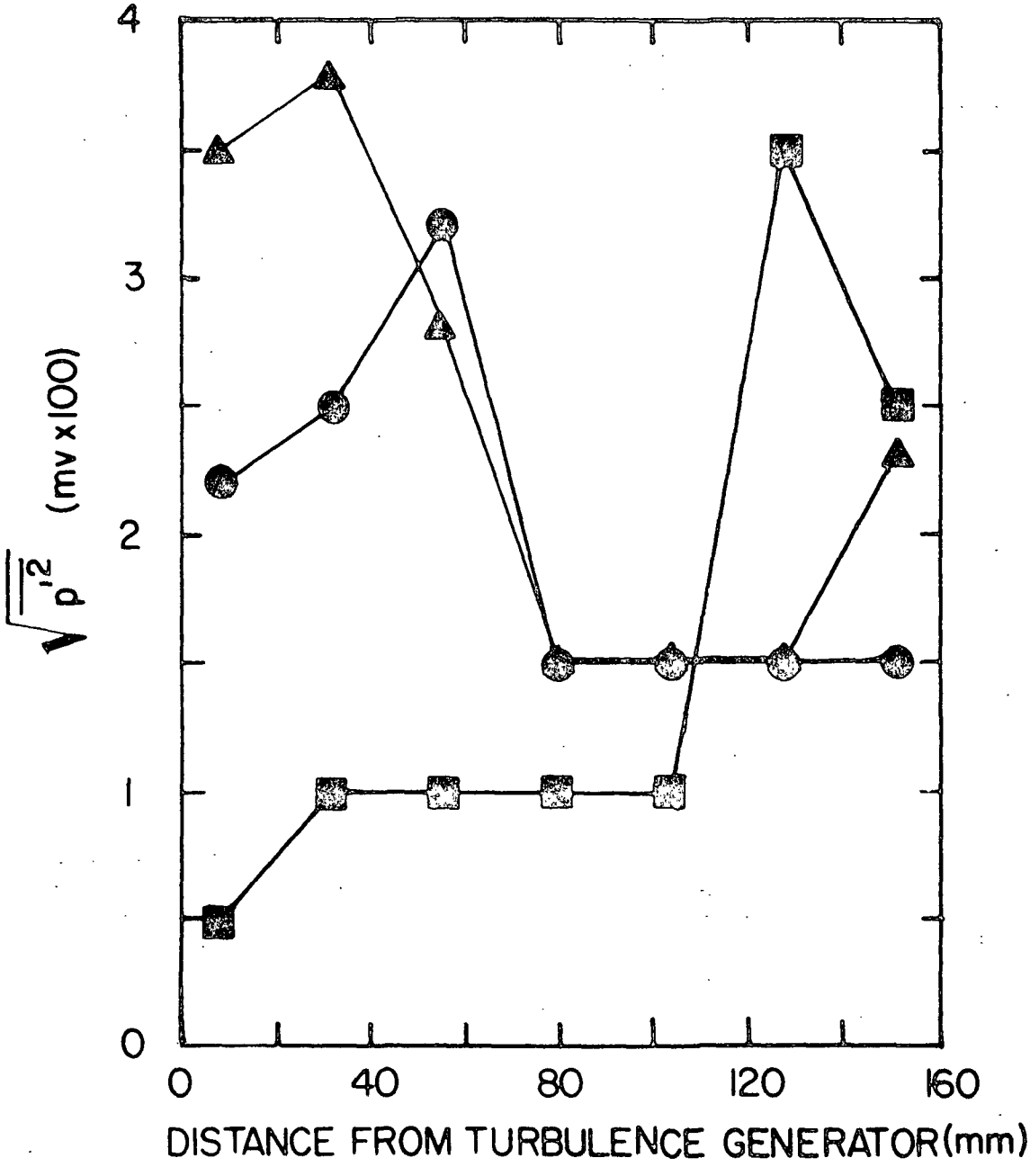

Figure 9. Intensity of pressure fluctuations as function of position downstream of turbulence generator for C = 1%, at $\bar{u}$ = 7.6 m/s (●), 9.1 m/s (▲), and 10.1 m/s (■).

EFFECT OF FIBER CONCENTRATION

The effect of increasing the fiber concentration was examined by comparing floc-size distribution curves at 9.1 and 10.2 m/s for C = 2% with the respective curves at C = 1%. At 7.6 m/s the size distributions obtained at this higher concentration were qualitatively the same as those for the 1% suspension, and therefore we need not discuss them here. Figures 10 and 11 show the size distribution curves at 9.1 and 10.2 m/s, respectively, for C = 2%. The corresponding intensities of the pressure fluctuations as functions of position downstream of the turbulence generator are plotted in Fig. 12.

Comparison of the size distribution curves in Fig. 10 with those in Fig. 7 indicates a somewhat unexpected effect of the higher fiber concentration in the disruption of flocs. For C = 1%, at $\overline{u}$ = 9.1 m/s, the number of the larger flocs increased as the suspension travelled across the turbulence generator (see Fig. 7). On the other hand, at C = 2%, these practically disappeared completely. This could have resulted because the flocs of increasing size associated with the higher fiber concentration may be easier to disrupt than smaller ones. The effect of the higher fiber concentration on the reflocculation process is also evident from the curves in Fig. 10. We notice that far downstream of the turbulence generator (probe 10) the fraction of the largest flocs increased considerably at the expense of the smallest ones, but the fraction of the latter remained considerably higher compared with the upstream size distribution (probe 1). At 10.1 m/s (Fig. 11), the breakup of flocs was qualitatively the same as for C = 1% at this same velocity, the difference being on the fraction of single fibers still apparent in curve 10 compared with curve 5. For C = 2%, a large fraction of the latter seems to still be present compared with the same curve for C = 1%.

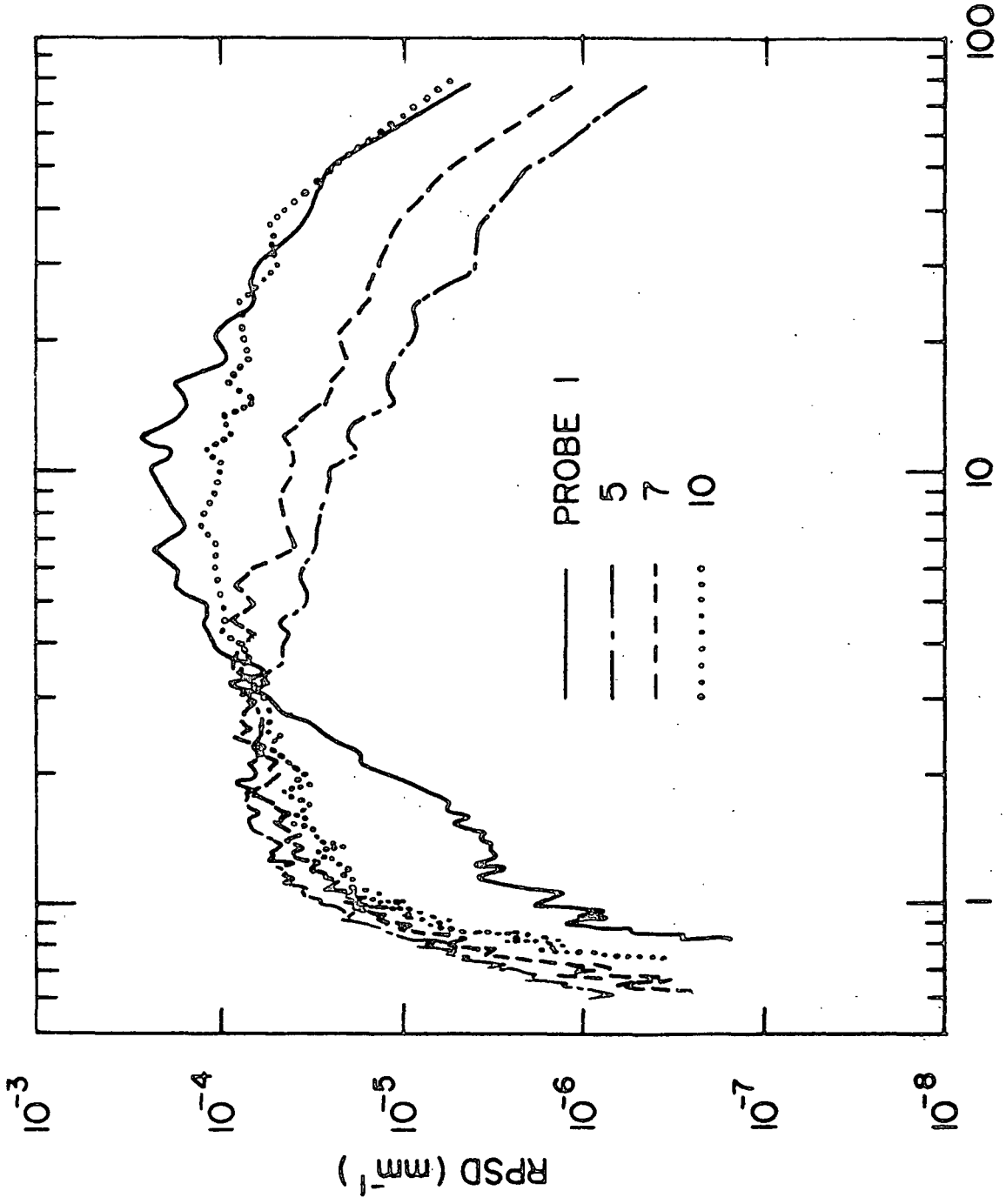

Figure 10. RPSD curves for C = 2% at $\bar{u}$ = 9.1 m/s.

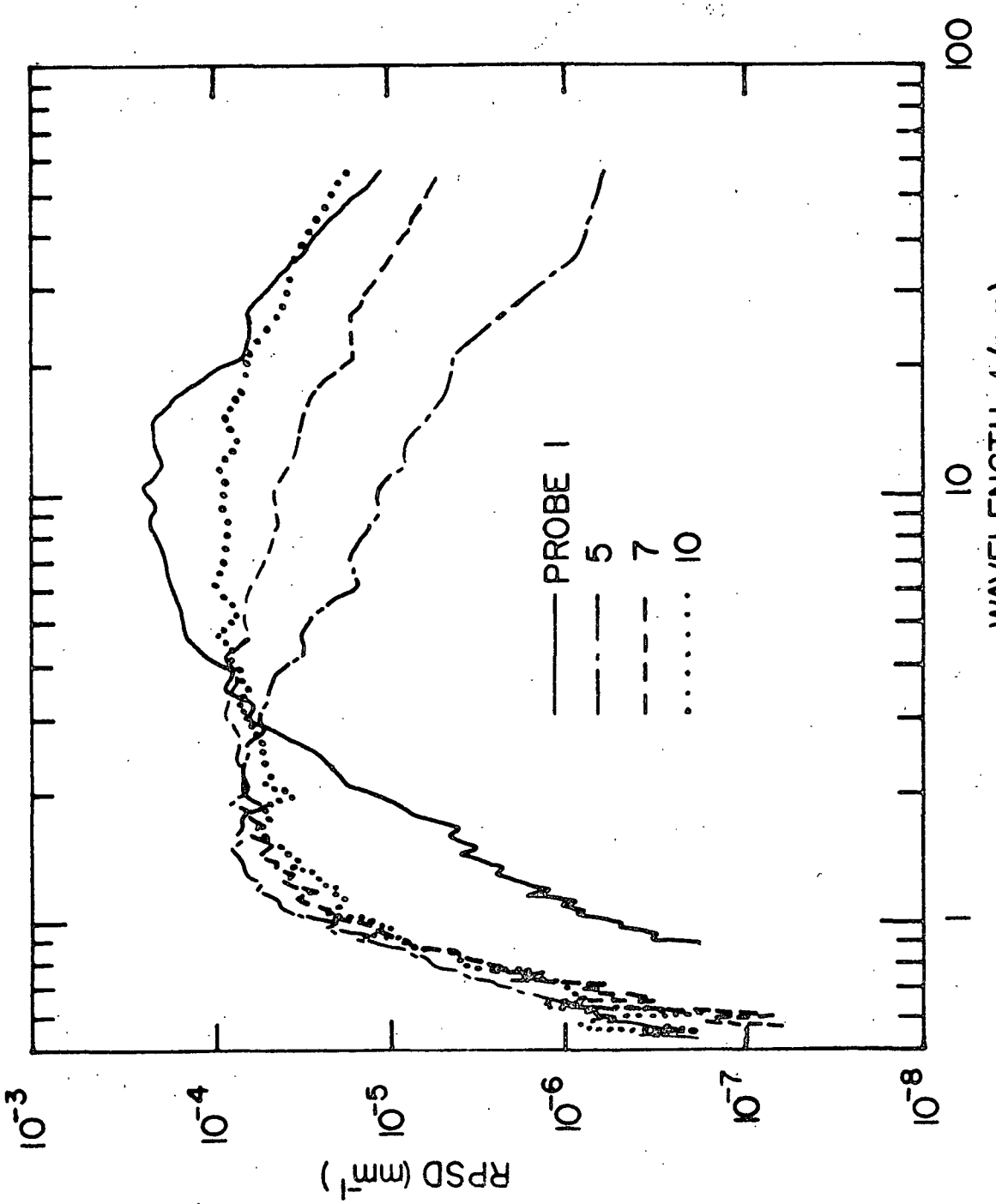

Figure 11. RPSD curves for C = 2% at $\bar{u}$ = 10.2 m/s.

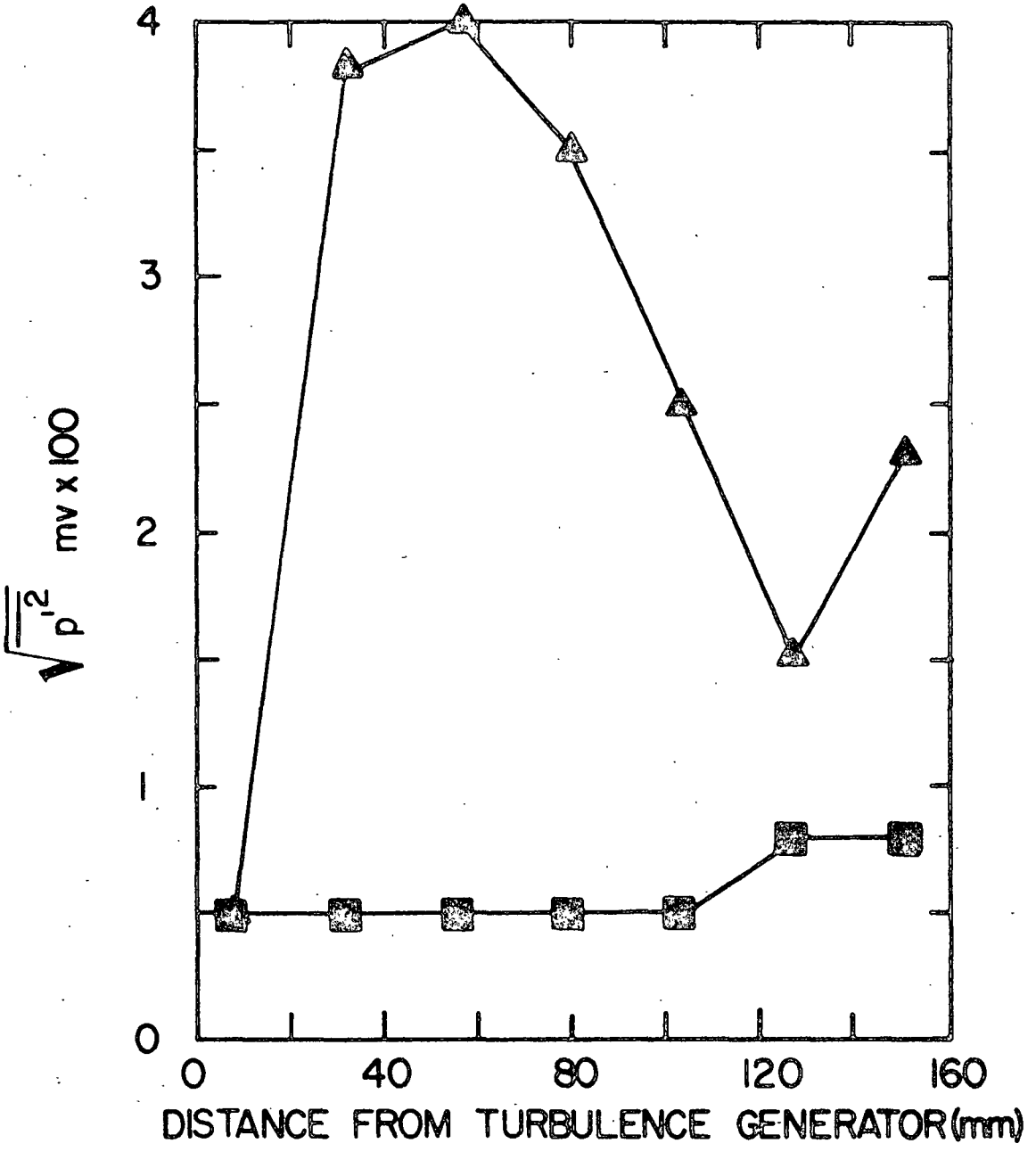

Figure 12. Intensity of pressure fluctuations as function of position downstream of turbulence generator for C = 2%, at $\bar{u}$ = 9.1 m/s (▲) and 10.1 m/s (■).

The intensity of the pressure fluctuations for C = 2% is presented in Fig. 12. At $\bar{u}$ = 9.1 m/s, the maximum in the pressure fluctuations occurs at the location of probe 7 ($\sim$ 55 mm) where curve 7 in Fig. 10 shows a significant increase in the fraction of the large flocs. The decrease downstream of probe 7 was likely due to the formation of uniform large flocs as indicated by curve 10 in Fig. 10. Tsuji and Morikawa (13) observed a similar behavior in the intensity of pressure fluctuations in systems of small solid particles being conveyed in an air stream. They show that as the average velocity decreased, the particles clustered to form aggregates and, consequently, the intensity of the pressure fluctuations increased. A further decrease in velocity resulted in the particles forming a uniform bed which was accompanied by less intense pressure fluctuations. At $\bar{u}$ = 10.1 m/s, the pressure fluctuations we measured remained uniform and low up to the last 25 mm of the test section, at which they slightly increased. At this velocity, still at the location of probe 10 (Fig. 11), a significant number of small flocs or fibers exist, whereas that of larger flocs did not reach the levels existing at probe 1.

The effect of increasing fiber concentration could not be completely elucidated from the size distribution curves presented here. At $\bar{u}$ = 9.1 m/s, for C = 2%, large, possibly uniform flocs seem to form faster compared with the 1% suspension judging from the pressure fluctuations. On the other hand, at $\bar{u}$ = 10.2 m/s, at the higher fiber concentration, the reflocculation was possibly retarded as indicated by comparing curve 10 in Fig. 8 and 11.

COHERENCE ANALYSIS

In the previous section, we examined the effects of average flow velocity and fiber concentration on the disruption of flocs across a turbulence generator and the reflocculation process as the turbulence decays. The flocculation results were presented as floc-size distribution curves both upstream and at various locations downstream of the turbulence generator. It was concluded from those results that increasing the fiber concentration enhances floc breakup, since the bigger flocs (likely to be three-dimensional) may be more inhomogeneous with respect to point-to-point fiber concentration and, therefore, have a higher occurrence of weak points at which they can fail. An additional effect of higher fiber concentration is the retardation of reflocculation at higher velocities. Increasing the average flow velocity, at a given fiber concentration, results in more effective disruption of flocs and a more dynamic reflocculation process. The flocculation measurements were complemented with measurements of the amplitude of pressure fluctuations at the wall of the flow channel, and both sets of measurements were consistent in characterizing the state of fluidization of the suspension.

In this section we examine the flocculation process downstream of a turbulence generator in the same experimental setup (see Fig. 1); however, rather than measure floc-size distribution curves from the power-spectral density functions we determine the probability of maintaining flocs of different sizes over the distance between two probes. This probability is obtained by calculating the coherence function between the signals from the two probes.

The coherence function γ^2_{xy} of two random signals x(t) and y(t), as a function of frequency f, is defined as (15)

$$\gamma^2_{xy}(f) = \frac{|G_{xy}(f)|^2}{G_x(f)\, G_y(f)} \qquad (5)$$

where $|G_{xy}(f)|$ is the magnitude of the cross-spectral density function of x(t) and y(t), and $G_x(f)$ and $G_y(f)$ are the power-spectral density functions of x(t) and y(t), respectively. Since $G_{xy}(f)$ is the Fourier transform of the cross-correlation function between x(t) and y(t), $\gamma^2_{xy}(f)$ is analogous to the cross-correlation coefficient and can be interpreted as the fraction of the mean square value of y(t) that was contributed by x(t) at each frequency. As defined in Eq. (5), $0 \leq \gamma^2_{xy}(f) \leq 1$; if $\gamma^2_{xy}(f) = 0$, the signals are incoherent or uncorrelated, but if $\gamma^2_{xy} = 1$, they are coherent. When either of these two limits exists at all frequencies, the signals are said to be either statistically independent or completely coherent.

For a given average velocity $\bar{u}$, each frequency is associated with a given floc size (wavelength) ℓ,

$$\ell = \bar{u}/f \qquad (6)$$

and, therefore, γ^2_{xy} can be expressed as a function of ℓ indicating the size range of the most stable flocs over the distance between two probes. Comparison of the coherence vs. wavelength curves for each pair of consecutive probes downstream of the turbulence generator allows (1) studying the development of stable flocs as a function of distance, (2) determining if the suspension attains a steady-state floc size distribution within the length of channel covered by the probes, and (3) establishing when single fibers, if these resulted from the breakup of flocs, cease being the most stable flocs. This last aspect can be used to set an upper limit for the distance (time) available for fiber alignment.

RESULTS FROM COHERENCE ANALYSIS

In this section we present the coherence functions for different average flow velocities and different fiber concentrations C. We first compare γ^2_{xy} between probes 1 and 5 located upstream and downstream of the turbulence generator, respectively, as a function of average flow velocity and fiber concentration. Figures 13 and 14 are plots of γ^2_{xy} *vs.* ℓ for C = 1% and 2%, respectively, at $\bar{u}$ = 5.1, 7.6, and 10.2 m/s. At 5.1 m/s, $0.15 \leq \gamma^2_{xy} \leq 0.6$, with the highest values at $\ell \geq 5$ mm, which indicates that the larger flocs were quite stable and were not disrupted. The curve for $\bar{u}$ = 7.62 m/s shows a local maximum coherence at $\ell \approx 7$-8 mm and an increase at 0.6 mm, while coherence is low at the high wavelength (large flocs). These results are consistent with those presented as curves 1 and 5 in Fig. 6. It was previously noted that as the suspension flows through the converging/diverging section, the relative number of flocs with $\ell > 10$ mm and $1.5 \leq \ell \leq 3$ mm increases appreciably, while those in the range $3 \leq \ell \leq 9$ mm experience only a slight decrease. Therefore, the signals from probes 1 and 5 should only have some coherence for $3 \leq \ell \leq 9$ mm as shown in Fig. 13. At $\bar{u}$ = 10.2 m/s, the results in Fig. 8 indicate that all flocs were completely disrupted, and consequently the signals from probes 1 and 5 should be uncorrelated at all frequencies. Such is the case as shown by the curve corresponding to 10.2 m/s in Fig. 13. For C = 2%, the coherence function curves in Fig. 14 behave similarly to those for C = 1% and are consistent with results from the PSD data in the earlier section.

Figures 15, 16, and 17 are plots of the coherence function *vs.* wavelength for every pair of consecutive probes downstream of the turbulence generator for a suspension with C = 1% traveling at $\bar{u}$ = 5.1 m/s, 7.6 m/s, and 10.2 m/s. Between probes 5 and 6, flocs of all sizes have, on the average, similar probability of existence, $0.1 \leq \gamma^2_{xy} \leq 0.25$. The coherence function curve for probes 6 and 7 as

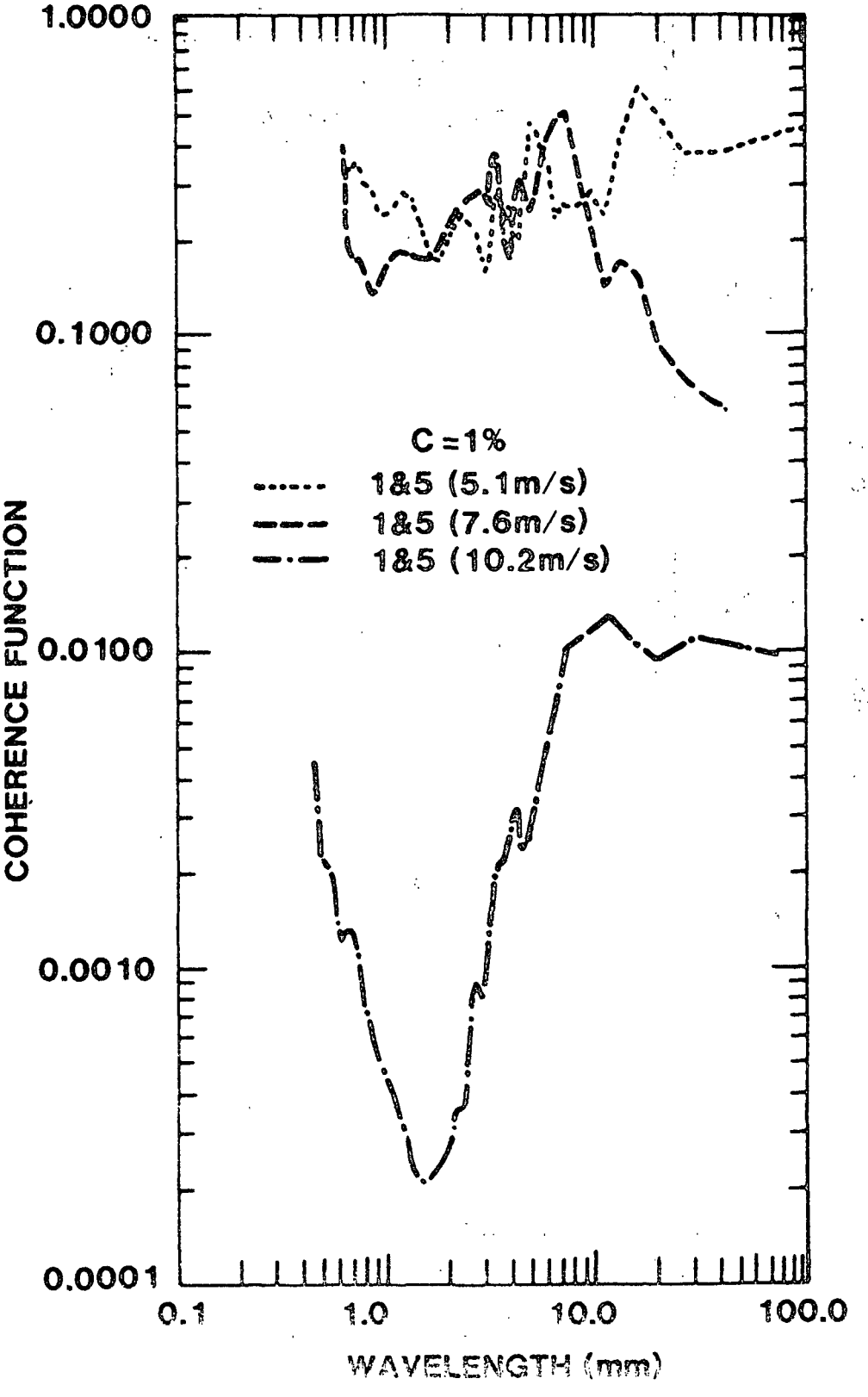

Figure 13. Coherence functions across the turbulence generator for $\bar{u}$ = 5.1 m/s, 7.6 m/s, and 10.2 m/s and C = 1%.

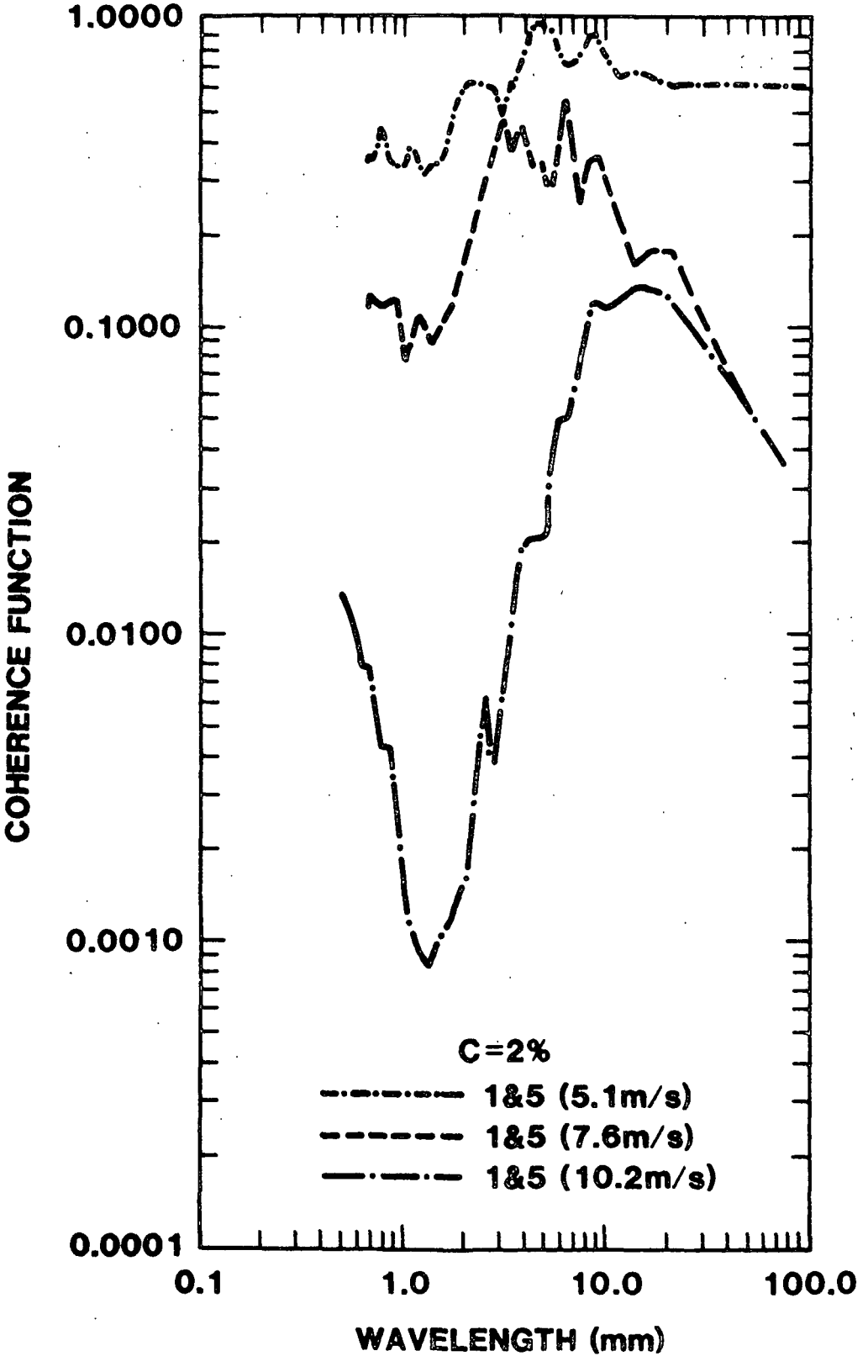

Figure 14. Coherence functions across the turbulence generator for $\bar{u}$ = 5.1 m/s, 7.6 m/s, and 10.2 m/s and C = 2%.

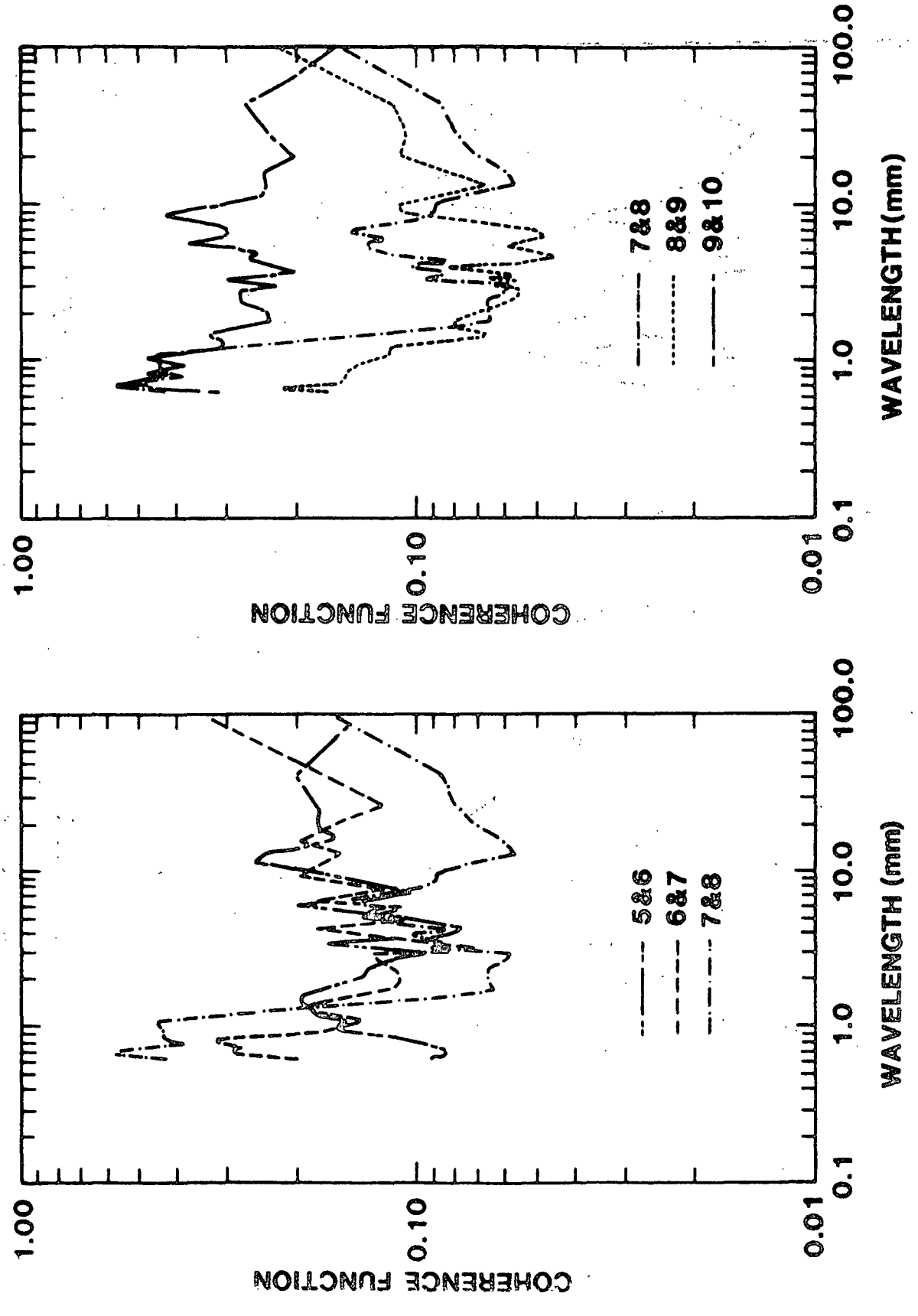

Figure 15. Coherence functions through the flow channel for $\bar{u}$ = 5.1 m/s, C = 1%.

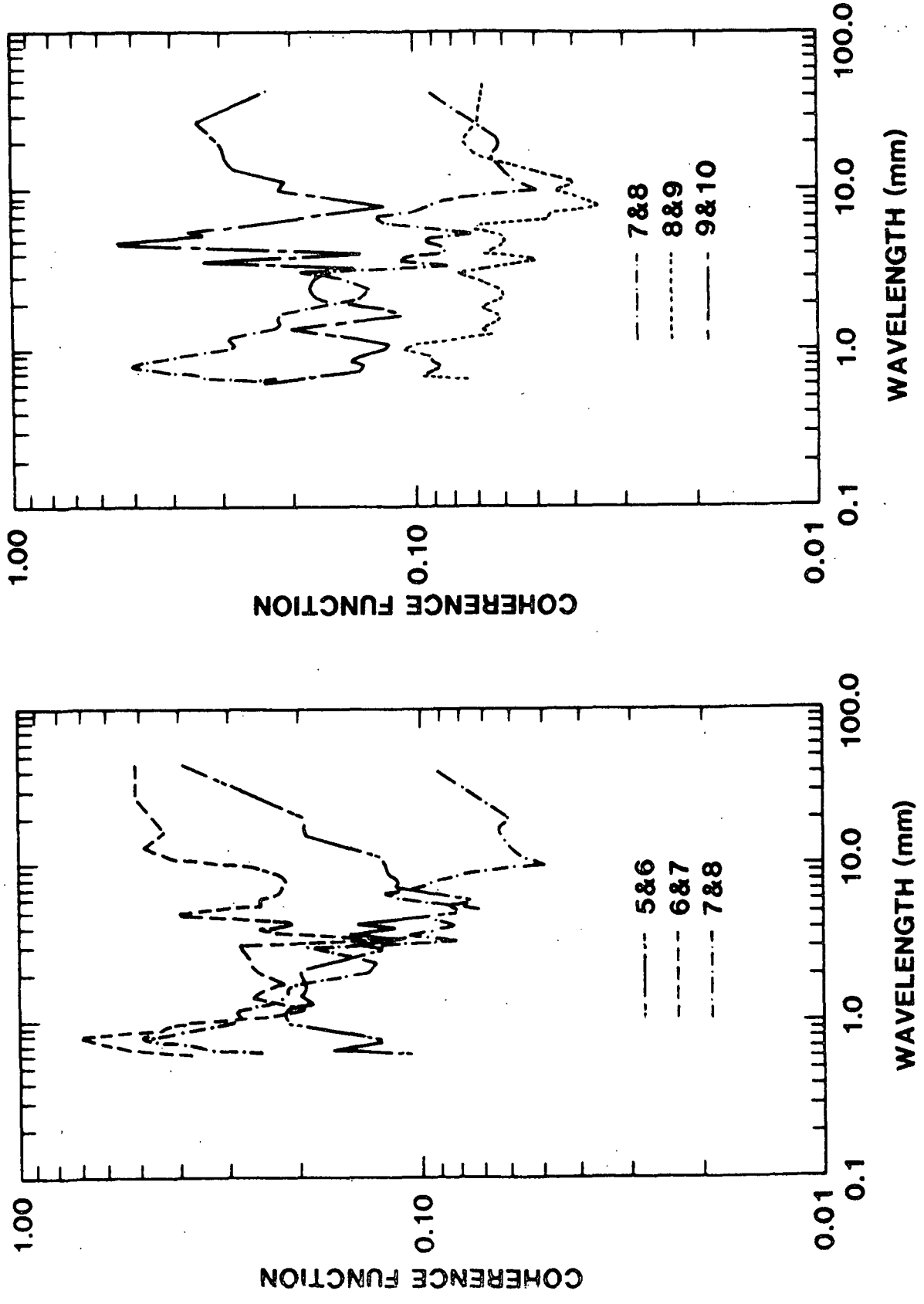

Figure 16. Coherence functions through the flow channel for $\overline{u}$ = 7.6 m/s, C = 1%.

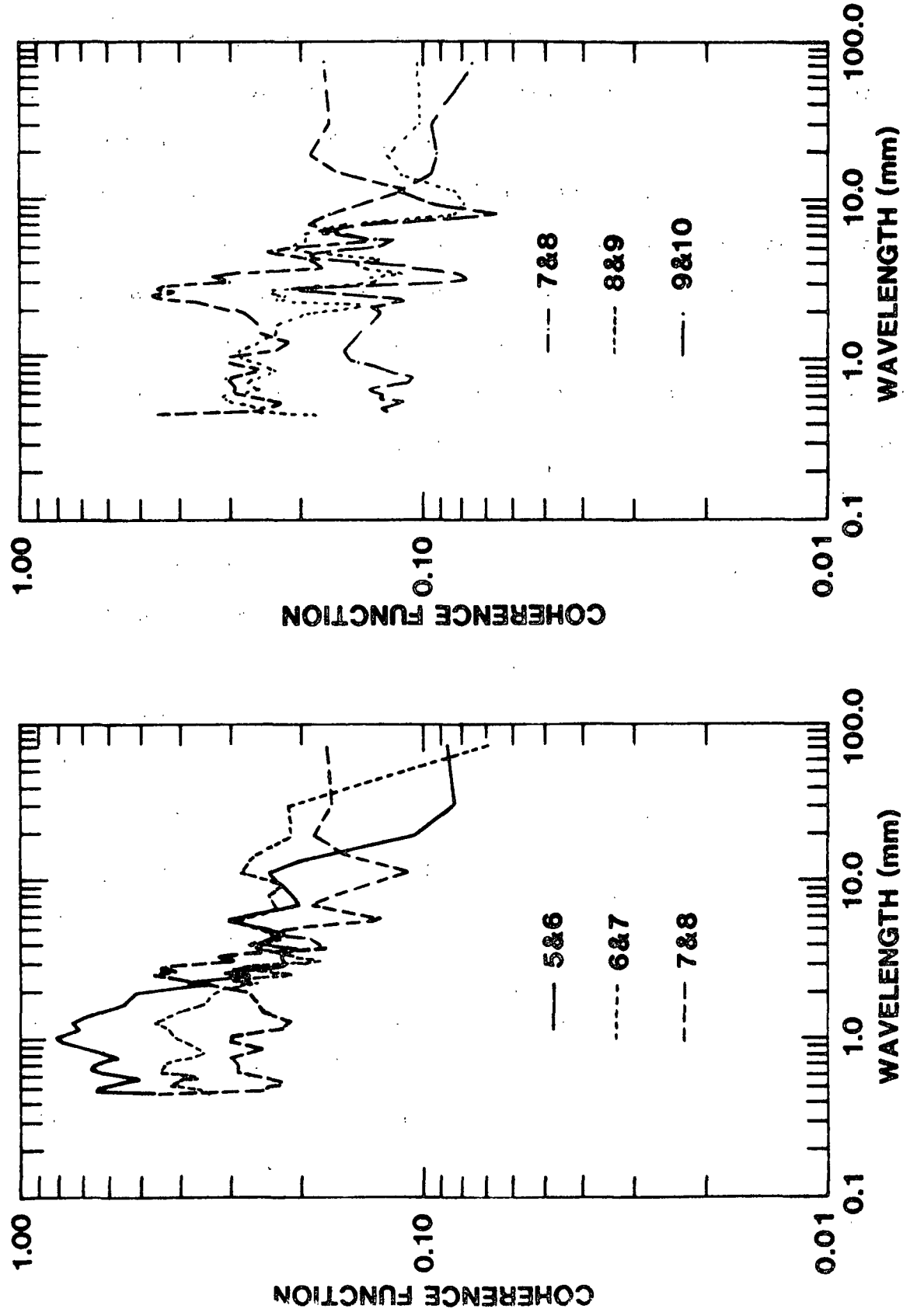

Figure 17. Coherence functions through the flow channel for $\bar{u}$ = 10.2 m/s, C = 1%.

well as that for probes 7 and 8 indicates that the coherence for the smallest flocs ($\ell < 2$ mm) increases while that of the largest ones decreases. It was observed in a previous section (Results from PSD Analysis) that at low velocities, large flocs downstream of the turbulence generator are generally disrupted. The curves in Fig. 15 show that over the distance between probes 6 and 8, the smallest flocs (fibers) are the most stable ones. As the suspension attempts to attain a steady-state floc-size distribution, the small flocs disappear by forming larger ones, and, therefore, their probability of existing between the two probes drops while for the latter rises as shown by the coherence function curve for probes 8 and 9. As a steady-state size distribution is attained, the coherence between probes 9 and 10 at all floc sizes increases.

Increasing the velocity to 7.6 m/s leds to the formation of large flocs as the suspension moved across the turbulence generator, thus, the curves shown in Fig. 16 exhibit initially (probes 5 and 6, and probes 6 and 7) large coherence at the larger wavelength indicating the stability of these flocs. As the suspension moves farther away from the turbulence generator, the large flocs are disrupted (Fig. 6); the signals of probes 7 and 8 are, therefore, uncorrelated at the frequencies corresponding to these flocs. As the suspension approaches a steady-state size distribution, the high coherence observed for the small flocs (fibers) between the locations of probes 6 and 7, and probes 7 and 8 drops between probes 9 and 10 due to these flocs forming larger aggregates. Between probes 8 and 9, all flocs have a low probability of being maintained; however, between probes 9 and 10 the coherence at all wavelengths increases with an outstanding maximum occurring at $\ell \approx 4.5$ mm. Because of the higher velocity the coherence over all wavelengths between probes 9 and 10 is not as uniform as for $\bar{u} = 5.1$ m/s.

The coherence function curves for C = 1% at $\bar{u}$ = 10.2 m/s are presented in Fig. 17. As was shown in the section on Results from PSD Analysis, at this velocity all large flocs were disrupted across the turbulence generator and mostly single fibers were observed immediately downstream of it. The coherence function curve for probes 5 and 6 shows flocs of approximately 1 mm to be the most stable ones (γ^2_{xy} > 0.8), while large flocs present at probe 5 disappear before reaching probe 6. The reflocculation process is evident from the curves corresponding to probes 6 and 7, and probes 7 and 8. In the former, the coherence at the short wavelengths drops while that at the longer ones increases. In the latter curve, both the coherence for the small and large flocs decreases and a definite peak appears at around 3 mm. The curves for probes 8 and 9, and probes 9 and 10 show evidence that the suspension has not reached a steady-state floc-size distribution. Comparing the curves for probes 9 and 10 at the three velocities corroborates the conclusion reached in the section on Results from PSD Analysis that at a higher velocity, a longer distance is required for the suspension to reach a steady-state size distribution. It is also evident from Fig. 17 that the distance available for fiber alignment is less than 8 mm or 1.6 ms, since the single fibers were the only ones with high coherence between probes 5 and 6.

At $\bar{u}$ = 5.1 m/s, increasing the fiber concentration from C = 1% to 2% (Fig. 18) results in the reflocculation process being less dynamic and an increase in the size of the most stable flocs immediately downstream of the turbulence generator. The curve for probes 5 and 6 in Fig. 15 has a maximum at about 11 mm, while the corresponding maximum in Fig. 18 is at 20 mm. Furthermore, no significant changes in the state of flocculation occur between probes 6 and 7 at C = 2%, and therefore a strong coherence is obtained at practically all wavelengths. Between probes 7 and 8, the larger flocs disappeared, and the most stable flocs are of the order of 1 mm.

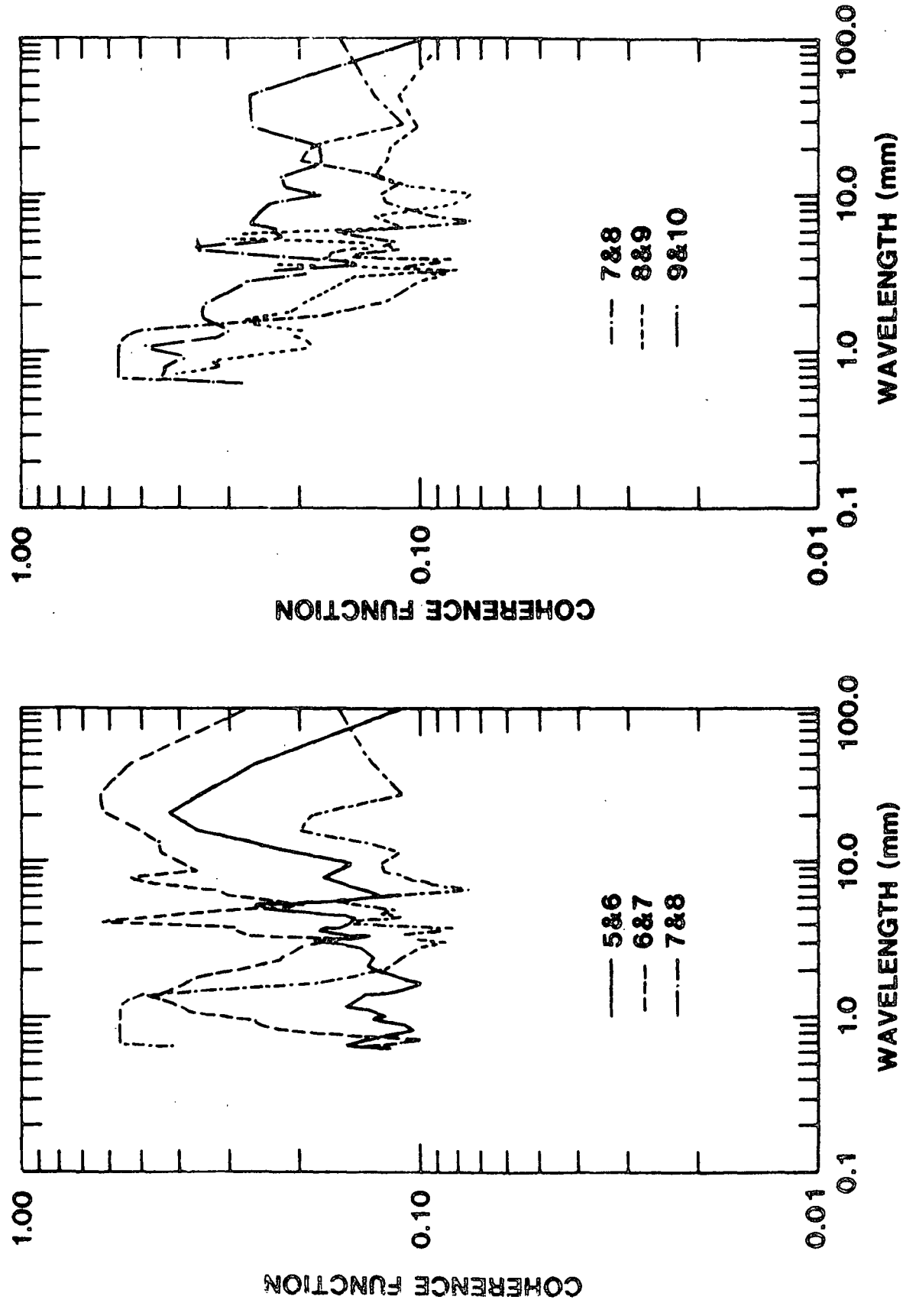

Figure 18. Coherence functions through the flow channel for $\overline{u}$ = 5.1 m/s, C = 2%.

As mentioned before, large flocs in more concentrated suspensions have a high probability of failure. Between 80 and 100 mm (probes 8 and 9) downstream of the turbulence generator, maximum coherence occurs for $3 \leq \ell \leq 5$ mm. By probe 9 the suspension has stabilized and the coherence of probes 9 and 10 at all wavelengths is similar to that obtained at C = 1%. Increasing the flow velocity of the 2% suspension to 7.6 m/s also leads to an increase in the number of flocs in the range $3 \leq \ell \leq 9$ mm. These flocs are not stable between probes 5 and 6 (Fig. 19); however, as smaller flocs (fibers) disappear due to the formation of larger aggregates these intermediate size flocs are once more quite stable between probes 6 and 7. As the suspension approaches a steady-state distribution, the intermediate size flocs disappear between probes 7 and 8, leading to stable floc sizes on the order of 1 mm. The coherence function curve for probes 8 and 9 is quite similar to that for probes 7 and 8. A fairly stable size distribution has been reached by probe 9, since the signals of probes 9 and 10 have $0.4 \leq \gamma^2_{xy} \leq 0.6$ at all floc sizes. The same curve for the 1% suspension shows coherence only at $\ell = 3$ mm.

The floc-size distribution curves in the section on Results from PSD Analysis for C = 2% at $\bar{u} = 10.2$ m/s show that immediately downstream of the turbulence generator most flocs are of single fiber size. The coherence function curves for the same conditions, Fig. 20, show that between probes 5 and 6 the size distribution is practically frozen since the coherence for $\ell \leq 10$ mm is $\gamma^2_{xy} \geq 0.6$, reaching a value of 0.97 at $\ell = 0.5$–0.6 mm. Further downstream (probes 6 and 7), these very small flocs (fibers) disappear and those of $\ell \approx 2$ mm become the most stable ones; however, compared with the curves in Fig. 17, at this higher fiber concentration, the coherence at all wavelengths still remains above 0.3 and for $1 \leq \ell \leq 10$ mm (mostly above 0.4) reaching values as high as 0.6. A significant change in the state of flocculation occurs between probes 7 and 8, and probes 8 and 9 as

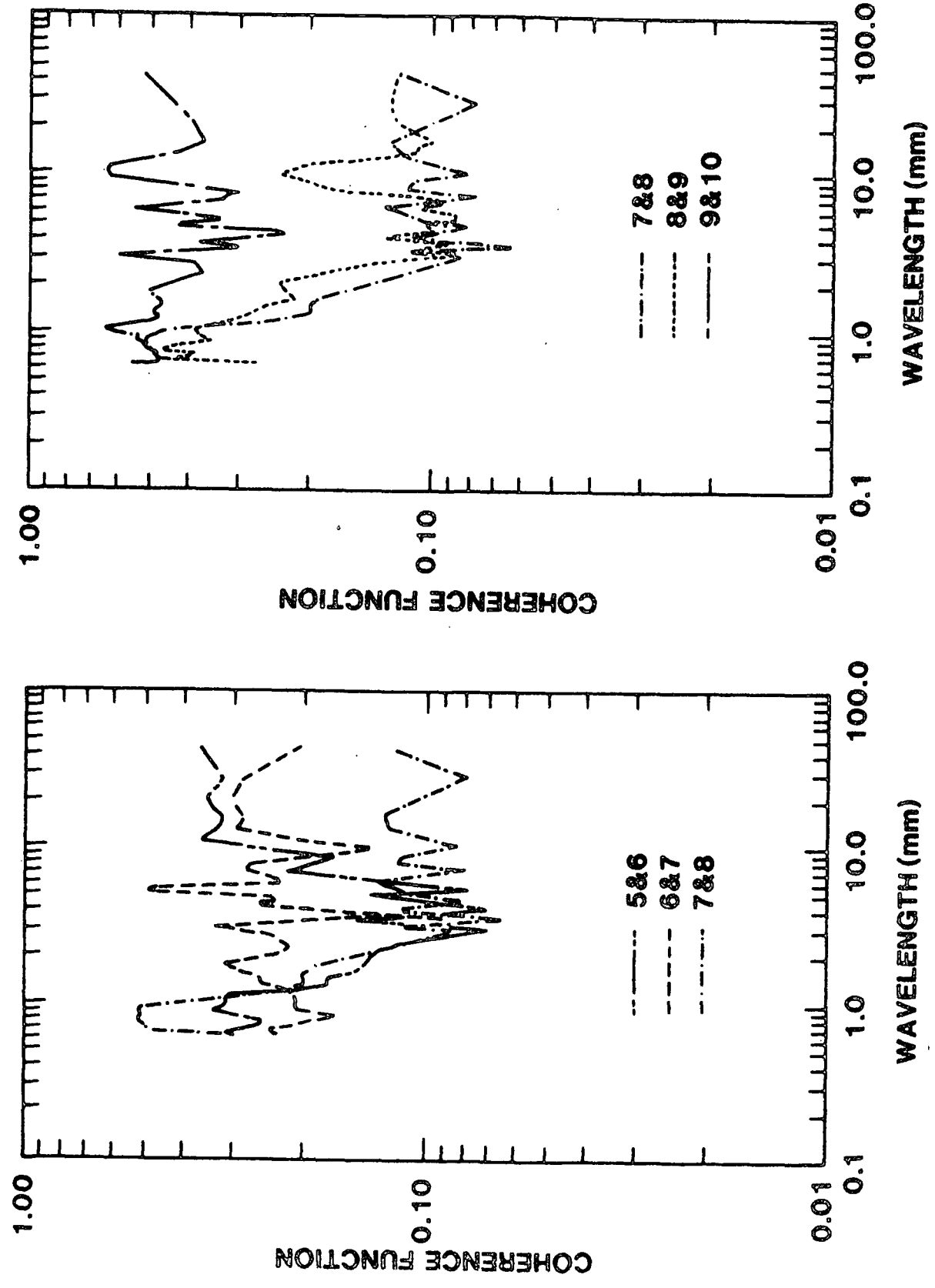

Figure 19. Coherence functions through the flow channel for $\bar{u}$ = 7.6 m/s, C = 2%.

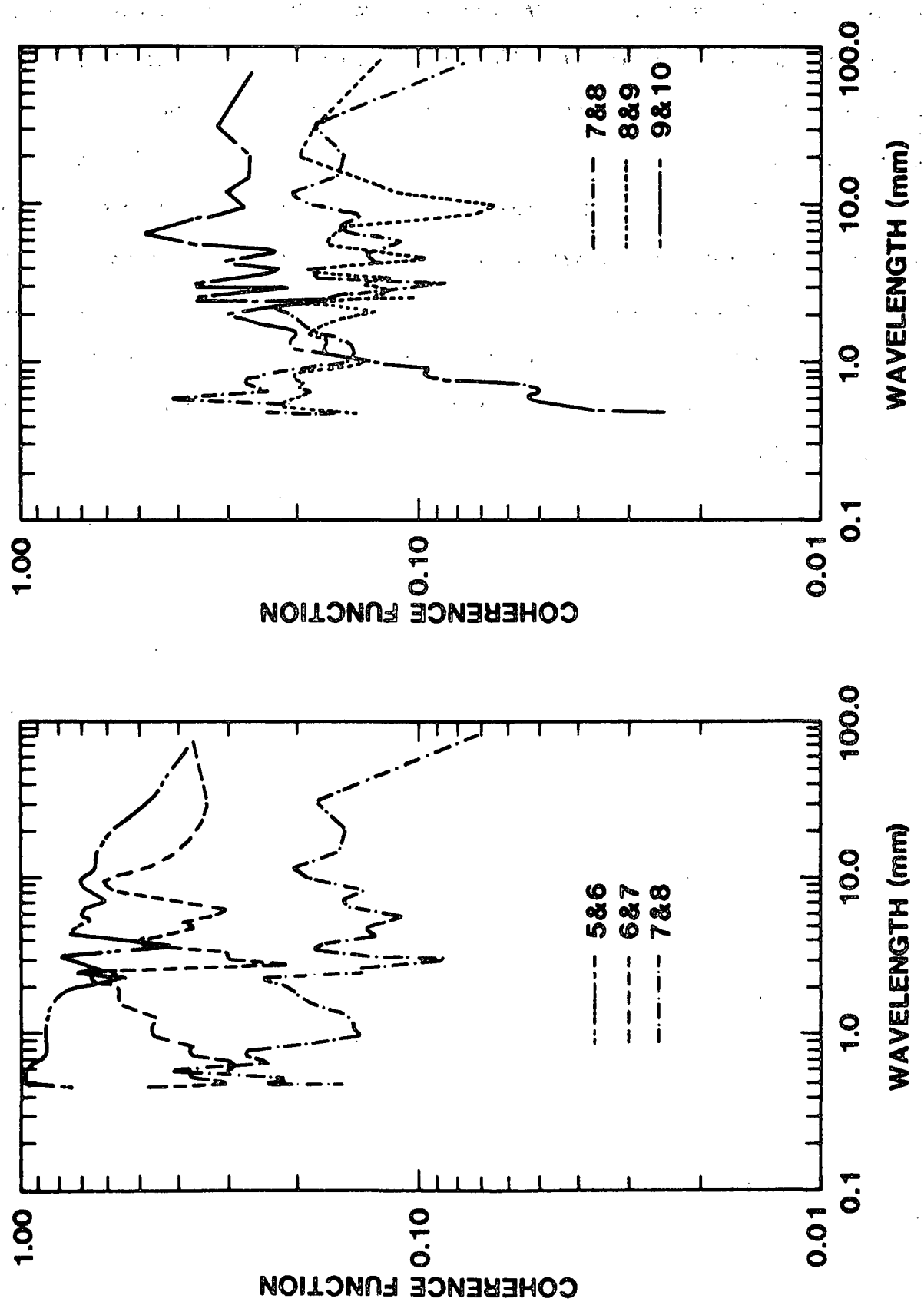

Figure 20. Coherence functions through the flow channel for $\overline{u}$ = 10.2 m/s, C = 2%.

evident from the sharp drop in the coherence observed. Possibly a fiber network is forming, since the coherence at large floc sizes between probes 9 and 10 increases considerably, but not to the values obtained between probes 5 and 6. It is clear that compared with the 1% suspension, the 2% one remains in a "frozen" state for a longer distance. The floc-size distribution curves in the section on Results from PSD Analysis for C = 2% and $\bar{u}$ = 10.2 m/s (Fig. 11) show a large number of single fibers still present at the location of probe 7. The results of both PSD and CF analysis seem to indicate that at these fiber concentrations and flow velocity conditions, the distance and time available for aligning fibers are of the order of 55 mm and 5.4 ms, respectively.

FIBER STRAIGHTENING AND ALIGNMENT

INTRODUCTION

The current state of the art in papermaking is based on sufficient dilution of the fiber suspensions to minimize fiber-fiber interactions that lead to the formation of fiber aggregates or flocs. Because of the large quantities of water that must be handled in a paper mill, the size of the papermaking equipment is excessively large. A possible avenue to reducing the size of such equipment, and consequently the capital intensiveness of the process as well as its operating costs, is to carry out the process using concentrated suspensions (2,3).

A major drawback of paper formed from concentrated suspensions is its poor mechanical properties compared to those of paper formed from dilute suspensions. This poor performance is primarily attributed to the lack of orientation of the fibers, which results in the formation of a felted structure. In conventional papermaking the fibers are oriented mainly in the plane of the paper, producing a layered sheet. To produce paper with acceptable properties from concentrated suspensions, the flocs must be disrupted and the fibers dispersed long enough to achieve alignment.

In previous sections, we have presented results of an experimental study which examined the effects of fiber concentration and average flow velocity on the disruption of fiber flocs via turbulence generation and the subsequent reflocculation as the turbulence decayed. We concluded from that study that an increase in fiber concentration positively affects floc breakup and may retard the reflocculation process or accelerate it depending on other conditions such as average flow velocity.

In this section we examine the effect of simple shear and elongational flows on the time evolution of the shape of a flexible but inextensible fiber in a concentrated suspension. We pay particular attention to the time required to align the fiber with the main direction of flow as a function of its initial shape. This should be an important consideration in the design of forming devices for making paper with desired properties from concentrated fiber suspensions.

MATHEMATICAL MODEL

The system under consideration here is a labeled fiber surrounded by a large number of other neighboring fibers as depicted in Fig. 21. Hinch (16) developed the equations of motion for an isolated flexible and inextensible thread suspended in a Stokes flow. Applying the slender-body approximation (large length-to-diameter ratio) to the inertialess thread, he obtained the expression

$$\frac{\partial \underset{\sim}{x}}{\partial t} = K_s \frac{\partial T}{\partial s} \frac{\partial \underset{\sim}{x}}{\partial s} + T K_n \frac{\partial^2 \underset{\sim}{x}}{\partial s^2} + \underset{\approx}{L} \cdot \underset{\sim}{x} \tag{7}$$

for the rate of change of the shape of the thread with time. The shape here is represented by a filament with position vector $\underset{\sim}{x}(s,t)$. Since the thread is inextensible, preservation of its arc-length at all times requires that the internal tension forces $T(s,t)$ within it balance the viscous forces preventing its motion, which leads to the equation

$$\frac{\partial}{\partial s}\left(K_s \frac{\partial T}{\partial s}\right) - k^2 K_n T = - \frac{\partial \underset{\sim}{x}}{\partial s} \cdot \underset{\approx}{L} \cdot \frac{\partial \underset{\sim}{x}}{\partial s} \tag{8}$$

with the tension subjected to the boundary conditions

$$T\ (\pm\ \ell,t) = 0 \qquad (9)$$

To solve Eq. (7) and (8) only the initial shape of the fiber $\underset{\sim}{x}\ (s,o)$ needs be prescribed.

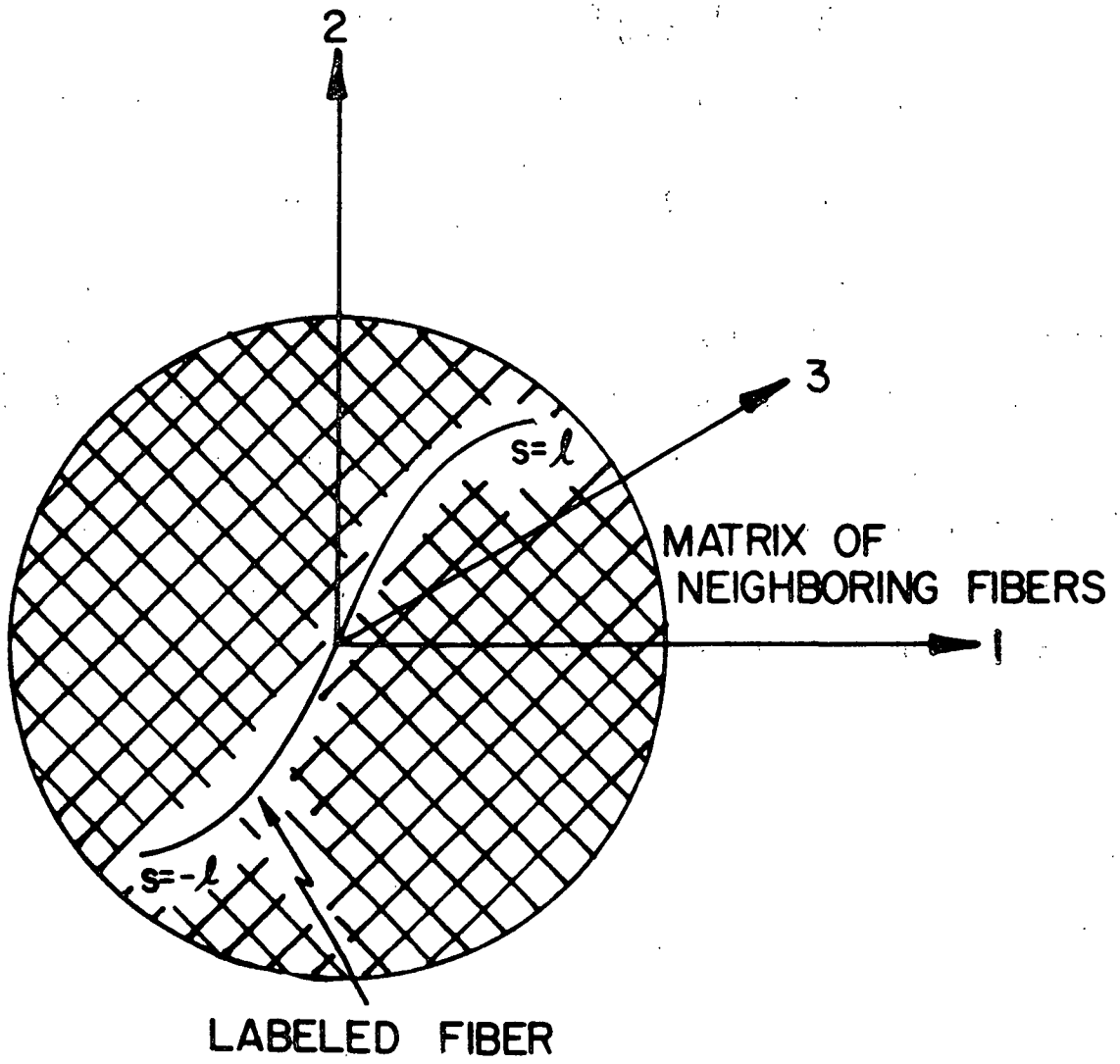

Figure 21. System considered: "labeled" fiber surrounded by large number of neighboring fibers.

The coefficients K_s and K_n in Eq. (7) and (8) are the longitudinal and normal components, respectively, of the mobility tensor $\underset{\sim}{K}$, which is the inverse of the hydrodynamic drag tensor $\underset{\sim}{R}$, that is,

$$\underset{\approx}{K} = [\underset{\approx}{R}]^{-1} \tag{10}$$

Goddard et al. (8) show that for concentrated suspensions of similar fibers of radius a,

$$\underset{\approx}{R} = N(s) \int_0^{2\pi} \int_0^{\pi} R'(s,\psi)\, F(s,\theta,\psi) d\psi d\theta \tag{11}$$

where $\underset{\approx}{R}'$ is obtained from lubrication theory as

$$\underset{\approx}{R}' = \frac{2\pi\mu a}{\sin\psi} \left[\frac{3}{2\varepsilon} \underset{\sim}{\delta}\,\underset{\sim}{\delta} + \ell n(\varepsilon^{-1}) \,(\underset{\approx}{I} - \underset{\sim}{\delta}\,\underset{\sim}{\delta})\right] \tag{12}$$

The function $F(s,\theta,\psi)$ in Eq. (11) is a probability distribution representing the fraction of neighboring fibers per unit length of the fiber of interest N(s) that lies between angular positions θ and $\theta + d\theta$ of the fiber with orientation between ψ and $\psi + d\psi$ with respect to the axis of the fiber, and ε is the dimensionless fiber-fiber separation normalized by the radius a. Substituting Eq. (12) into (11), inverting the latter, and recognizing that

$$K_s = \frac{\partial \underset{\sim}{x}}{\partial s} \cdot \underset{\approx}{K} \cdot \frac{\partial \underset{\sim}{x}}{\partial s} \tag{13}$$

and

$$k^2 K_n = \frac{\partial^2 \underset{\sim}{x}}{\partial s^2} \cdot \underset{\approx}{K} \cdot \frac{\partial^2 \underset{\sim}{x}}{\partial s^2} \tag{14}$$

we get

$$K_s = \frac{1}{2\pi\mu a N \ell n(\varepsilon^{-1})} \left\{\int_0^{2\pi} \int_0^{\pi} \frac{F(s,\theta,\psi)}{\sin\psi} d\psi d\theta\right\}^{-1} \tag{15}$$

and

$$K_n = \frac{\varepsilon}{3\pi\mu a N} \left\{\int_0^{2\pi} \int_0^{\pi} \frac{F(s,\theta,\psi)}{\sin\psi} d\psi d\theta\right\}^{-1} \tag{16}$$

The ratio of the normal to the longitudinal component of $\underset{\approx}{K}$ is then

$$\frac{K_n}{K_s} = \frac{2}{3}\,\varepsilon \ell n(\varepsilon^{-1}) \tag{17}$$

Goddard and Huang (17) proposed that in the limit $\varepsilon \ln(\varepsilon^{-1}) \to 0$, the normal component of the mobility is negligible with respect to the longitudinal component, reducing Eq. (7) and (8) to

$$\frac{\partial \underset{\sim}{x}}{\partial t} = K_s \left(\frac{\partial T}{\partial s}\right) \frac{\partial \underset{\sim}{x}}{\partial s} + \underset{\approx}{L} \cdot \underset{\sim}{x} \tag{18}$$

and

$$K_s \frac{\partial^2 T}{\partial s^2} = - \frac{\partial \underset{\sim}{x}}{\partial s} \cdot \underset{\approx}{L} \cdot \frac{\partial \underset{\sim}{x}}{\partial s} \tag{19}$$

respectively, where for circular fibers of constant cross section, K_s is constant. Thus, Eq. (18) and (19) represent the motion of a thread that is being hindered by the presence of a large number of neighboring fibers. This model can be considered analogous to the reptation model of Doi and Edwards (18,19) for the motion of a given polymer chain in a concentrated melt.

For a concentrated suspension of dispersed fibers Wahren (3) obtained the following expression for ε,

$$\varepsilon = [\ell n(\alpha) + 1.27324]^{1/2}\,[\sqrt{\pi/C_v} - 2] \tag{20}$$

where C_v is the volume concentration of fibers of length-to-diameter aspect ratio α. Equation (20) indicates that ε decreases rapidly with increasing concentration and approaches zero at $C_v \approx 0.7855$. Using this equation the ratio of the normal to longitudinal components of the fiber mobility given in Eq. (17) can be calculated

and the validity of the asymptotic Eq. (18) and (19) as function of fiber concentration can be established. In Fig. 22 we present the value of this ratio as a function of the fiber concentration for $\alpha = 100$ and 300. First, estimation of the mobility of a fiber for concentrated suspensions using the lubrication theory approach of Goddard et al. (15) must be restricted to concentrations for which $\varepsilon < 1$ since K_S must not be negative [Eq. (15)]. In Fig. 22, $\varepsilon < 1$ at $C_V \approx 0.555$ for $\alpha = 100$, and at approximately 0.59 for $\alpha = 300$. It is also shown in this figure that K_n/K_S drops very sharply for $C_V > 0.75$, since in the product $\varepsilon \ell n(\varepsilon^{-1})$, ε approaches 0 faster than $\ell n(\varepsilon^{-1})$ goes to infinity. The initial increase in the curves is due to a faster increase in $\ell n(\varepsilon^{-1})$ than a decrease in ε. It is clear from these curves that in both cases ($\alpha = 100$ and 300) the assumption of negligible mobility normal to the fiber axis should not be invoked for $C_V < 0.75$.

We do not attempt here to estimate values of K_S and K_n using Eq. (15) and (16) for different values of the parameters because of the singularity in the value of the integrand at $\psi = 0$ and $\pi/2$ in these equations. We choose arbitrary values of K_S, and when solving Eq. (7) and (8) instead of (18) and (19), K_n is evaluated using Eq. (17) for given values of C_V and α.

We consider in this study the two-dimensional evolution of the shape of the labeled fiber when the suspension is subjected to a simple shear flow for which

$$\underset{\approx}{L} = \begin{bmatrix} 0 & \gamma_S \\ 0 & 0 \end{bmatrix} \tag{21}$$

and a simple elongation flow for which

$$\underset{\approx}{L} = \begin{bmatrix} \gamma_E & 0 \\ 0 & -\gamma_E \end{bmatrix} \tag{22}$$

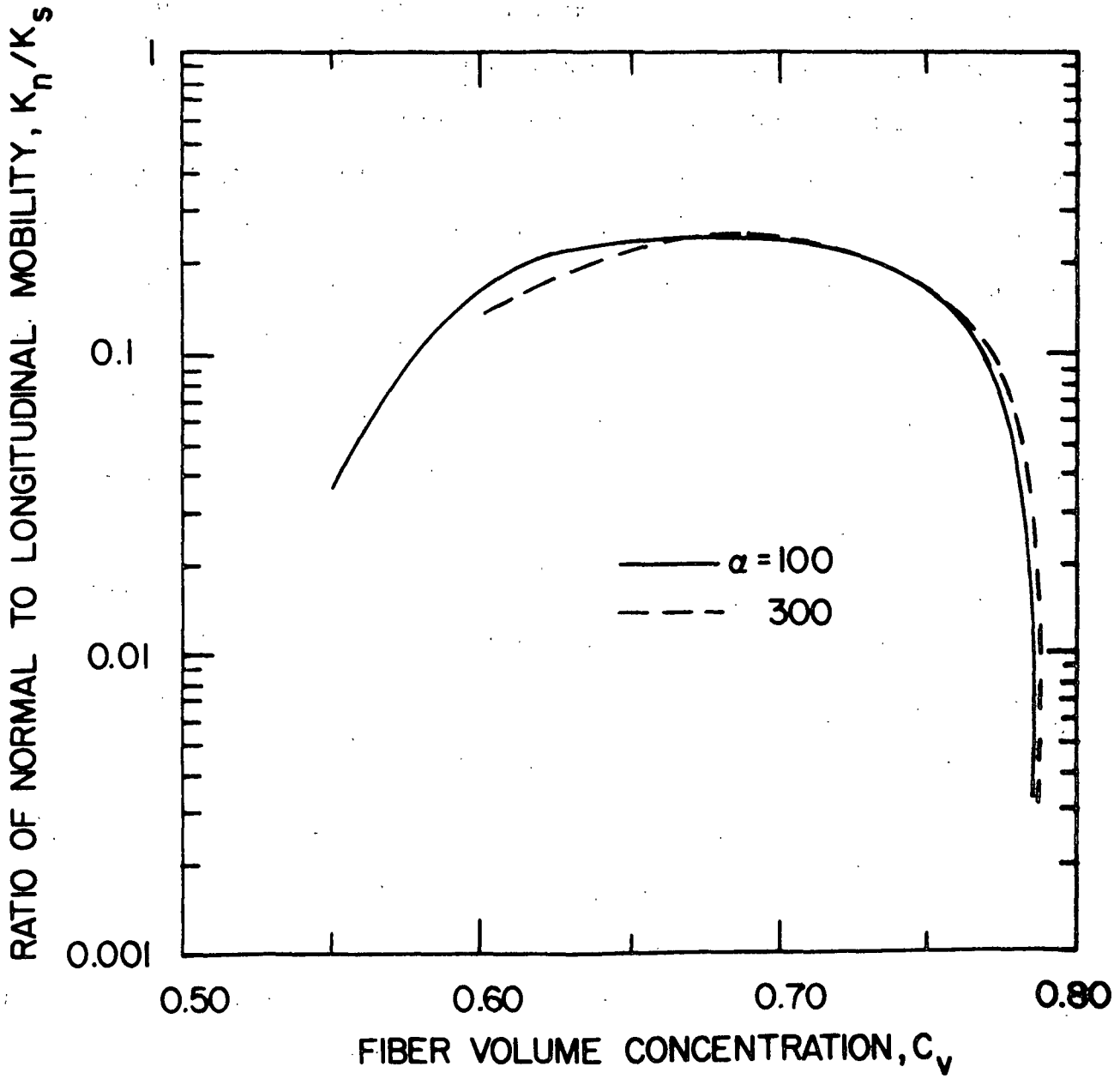

Figure 22. Ratio of K_n/K_s as function of fiber volume concentration for α = 100 and 300, respectively.

SOLUTION PROCEDURE

Equations (7) and (8) do not allow for an analytical solution and therefore they are solved numerically. For the asymptotic Eq. (18) and (19), Goddard and Huang (17) show that a closed-form analytical solution is possible. However, obtaining this solution requires a rather complex transformation from the independent variable s along the arc-length of the fiber to the material points of the continuum surrounding it. Because this transformation does not render the analytical solution suitable for modelling the evolution of the shape of the fiber as function of its initial shape, we also solve Eq. (18) and (19) numerically.

The fiber of length 2ℓ is divided into fifty (50) elements of equal length Δs. A fourth-order Runge-Kutta scheme is used to calculate the value of $\underset{\sim}{x}$ at the end points of each element as a function of time. The derivatives at each point s_i along the arc-length, $(\partial \underset{\sim}{x}/\partial s)_{s_i}$ and $(\partial^2 \underset{\sim}{x}/\partial s^2)_{s_i}$, are evaluated using a Langrangian interpolating polynomial of degree 4. The equation for the tension T along s is solved using Orthogonal Collocation of Hermite Cubic Polynomials on Finite Elements. Details on this technique are provided by Finlayson (20).

Similarly to Hinch (16), we chose to rescale the length of each element along the fiber to Δs after each time step without changing its direction to compensate for the error introduced by the explicit solution of the shape equation on the total length of the fiber, and to maintain the center of mass of the fiber fixed in order to facilitate the comparison of its shape at different times. The error in the fiber length after rescaling each element length was of the order of $10^{-3}\%$ at all times. A time step of the order of 10^{-4} second was found to be suitable, since decreasing it by an order of magnitude did not change the outcome of the calculations.

The solution procedure used was the following:

1. Specify initial fiber shape $\underset{\sim}{x}(s,0)$.
2. Calculate the tension T using Eq. (8) or (19).
3. Solve for new shape $\underset{\sim}{x}(s, t + \Delta t)$ using Eq. (7) or (19).
4. Rescale length of each element to Δs.
5. If time is less than the maximum prescribed time return to Step 2; if not, terminate computations.

RESULTS

The numerical scheme described above was tested using an initially straight thread, which according to Hinch (16), and Goddard and Huang (17), should behave like a rigid rod, that is, remain undeformed. In Fig. 23, part a, we present the evolving shape of the straight fiber for the case of simple shear flow. Identical results were obtained using Eq. (7) and (8), and Eq. (18) and (19). The shape of the fiber is shown in terms of a dimensionless time τ (= $t\gamma_S$) and the arrow indicates the main direction of flow. Part b of Fig. 23 presents the evolution of the shape of the initially straight fiber obtained using Eq. (18) and (19) for the case of simple elongational flow in terms of τ^* (= $t\gamma_E$). In both flow fields the fiber remained straight, the difference being in the time required for it to align with the flow; in the elongational flow it occurs faster if γ_S and γ_E are of the same magnitude.

It should be mentioned here that in shear flows the fiber rotates, but as a result of the slender-body approximation this couple is eliminated [Hinch, (16)] and once the fiber aligns with the flow it will remain in that orientation. However, the period of rotation of the fibers tends to be long as the aspect ratio, α goes

to infinity, and the solution obtained for shear flows should be close to the true orientation of the fiber. Furthermore, Hinch's analysis shows that the distortions introduced when terms of order α^2 are included in the shape of a straight fiber decay rapidly enough and the fiber does not rotate through the flow.

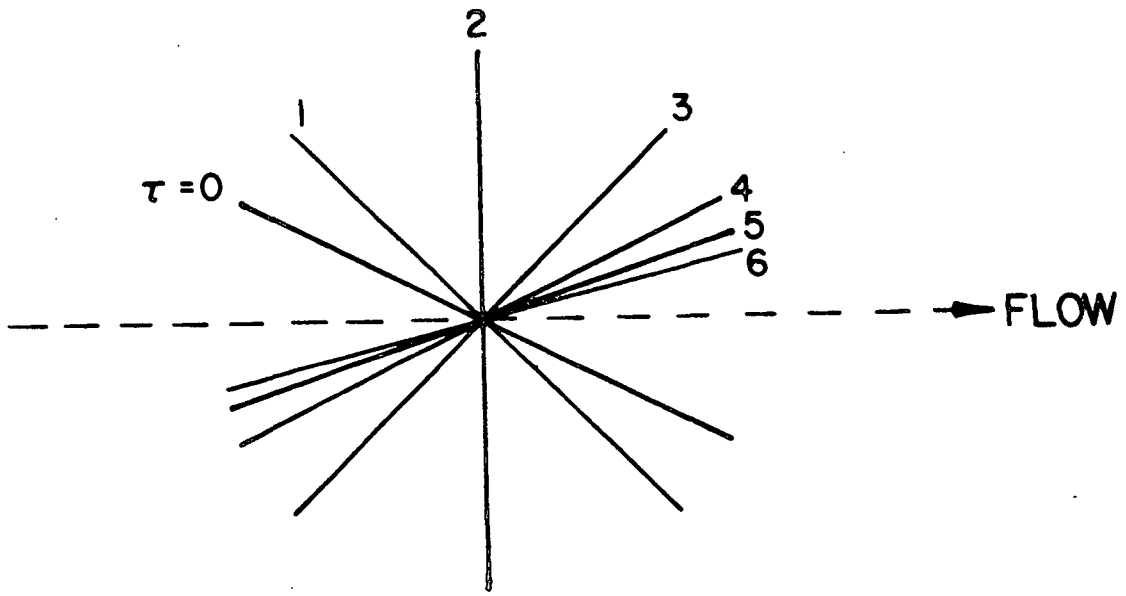

Part a

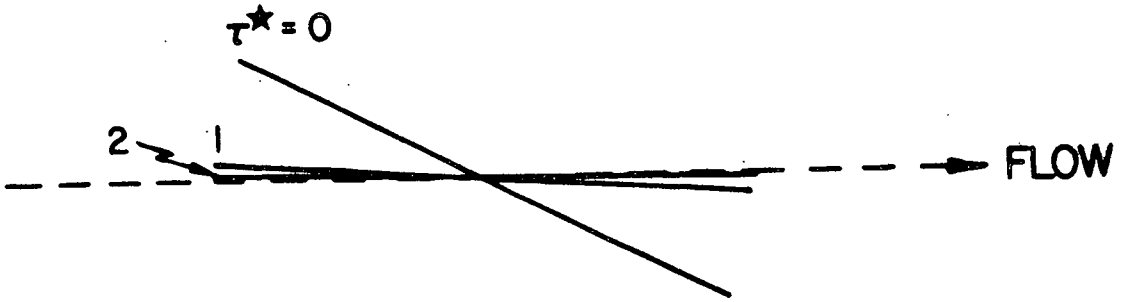

Part b

Figure 23. Evolving shape of straight fiber in simple shear flow (Part a) and simple elongational flow (Part b).

We also tested the validity of the approximation of Goddard and Huang (17) for concentrated suspensions for a fiber positively oriented in a shear flow. Parts a and b of Fig. 24 show the evolution of the shape of the fiber for the Goddard-Huang approximation [Eq. (18) and (19)] and the solution of Eq. (7) and (8), respectively. Equations (7) and (8) were solved for $C_v = 0.75$ and $\alpha = 300$ giving $K_n/K_s = 0.172$. The two solutions are, for all intended purposes, identical. As we shall indicate later, this is true only if the curvature of the fiber is not large. The general features of the solution are not changed dramatically in any case when using Eq. (18) and (19) instead of (7) and (8). Because solving Eq. (18) and (19) required less computing time than Eq. (7) and (8), we used the former two equations for the purpose of establishing the effect of the flow field.

Comparison of Part c of Fig. 24 (elongational flow) to Part a demonstrates the effect of the flow field on straightening the fiber and aligning it with the flow. Similar to the straight fiber in Fig. 23, the time required to align the fiber is approximately $\tau^* = 2$ with the elongational flow. In the shear flow, at $\tau = 3$ the fiber is straight but its axis is at 15° from the horizontal (flow direction). In Fig. 25 we make a similar comparison for a fiber whose initial shape is negatively oriented with the flow. In this case the elongational flow also practically aligns the fiber by $\tau^* = 2$, while in the shear flow at $\tau = 4$ the fiber is not yet straight and is oriented at about 20° from the direction of flow.

In Fig. 26 and 27 we show similar comparisons for fibers with initially negative and positive orientations, respectively, but less inclined than those in Fig. 24 and 25. The different shapes of the fiber in Part a of Fig. 26 indicate that the tendency for the fiber in a shear flow is to straighten ($\tau = 1$) before it is oriented with the flow. At $\tau = 3$, this fiber has essentially the same shape and orientation as that in Part b of Fig. 24. In elongational flow (Fig. 26, Part b)

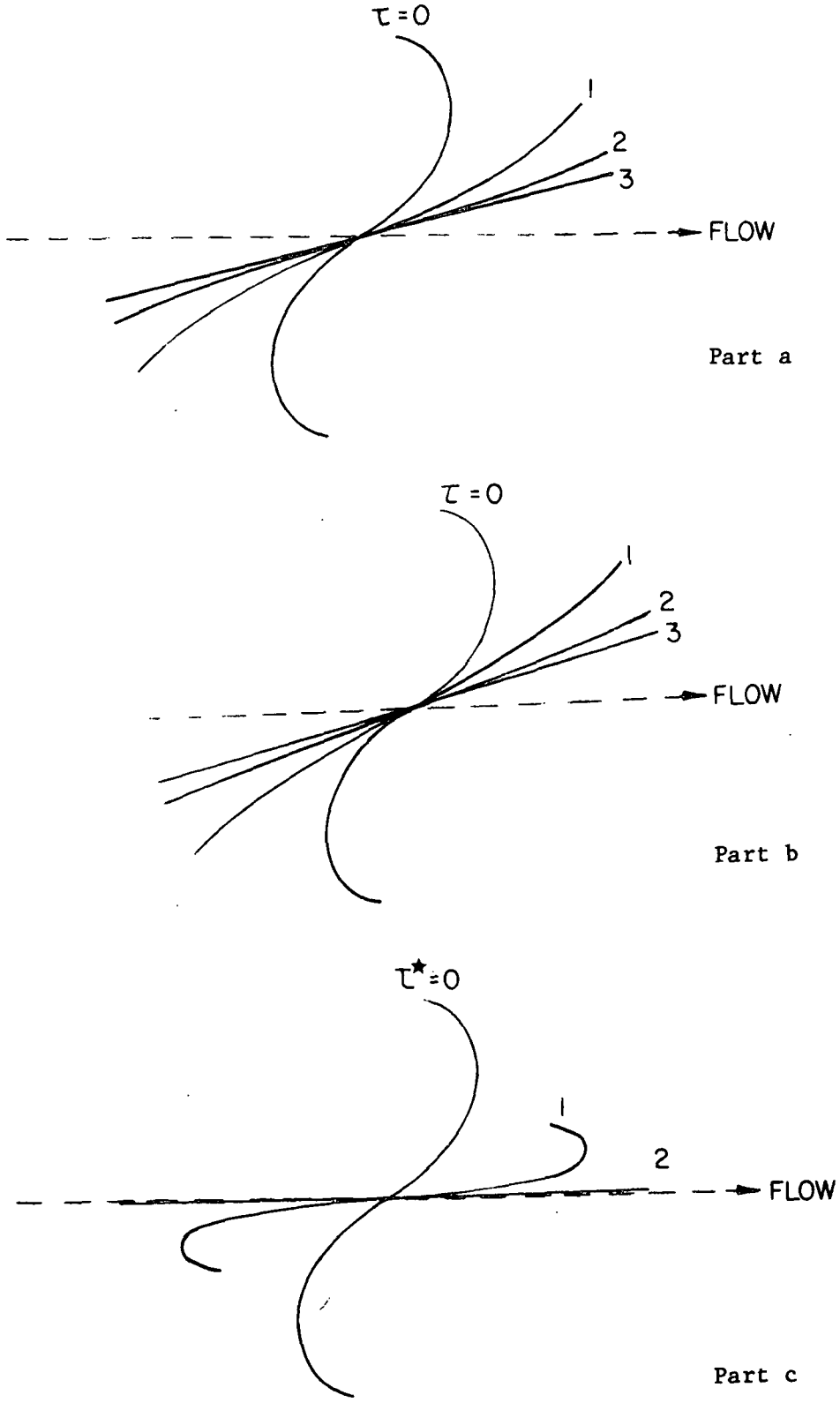

Figure 24. Evolving shape of initially positively oriented fiber in simple shear flow using Goddard-Huang approximation (Part a), Eq. (1) and (2) with K_n/K_s = 0.172 (Part b), and simple elongational flow (Part c).

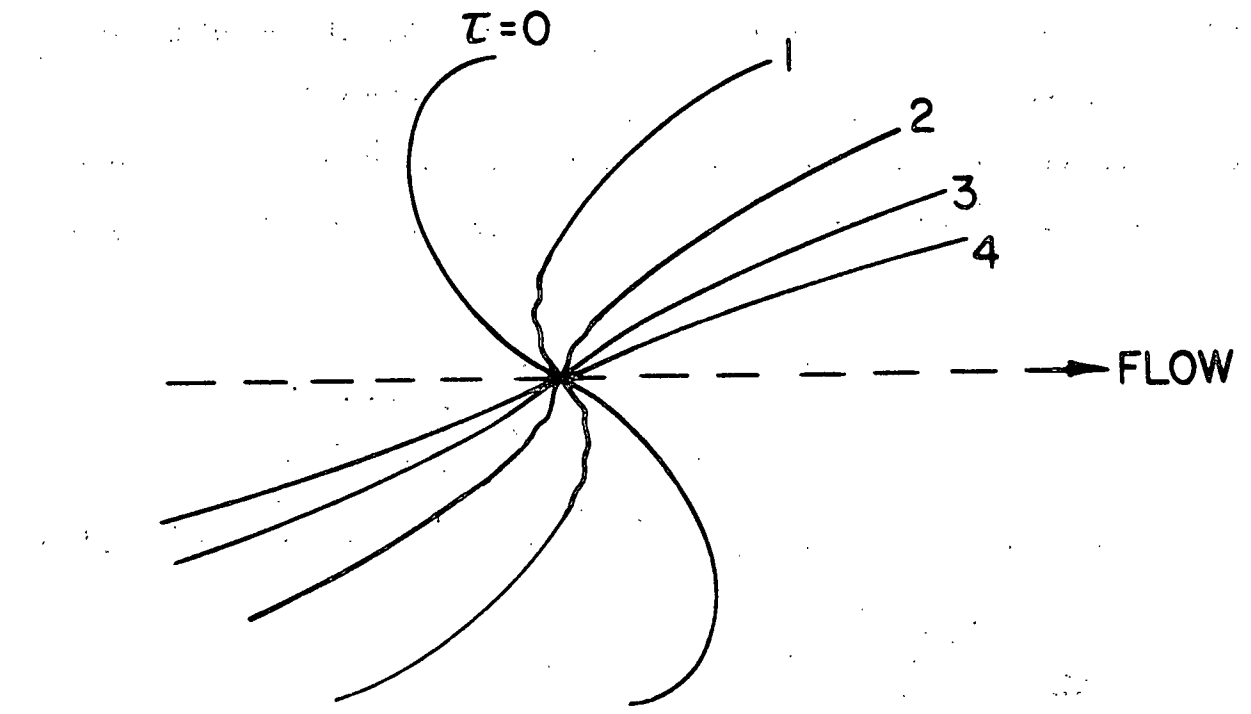

Part a

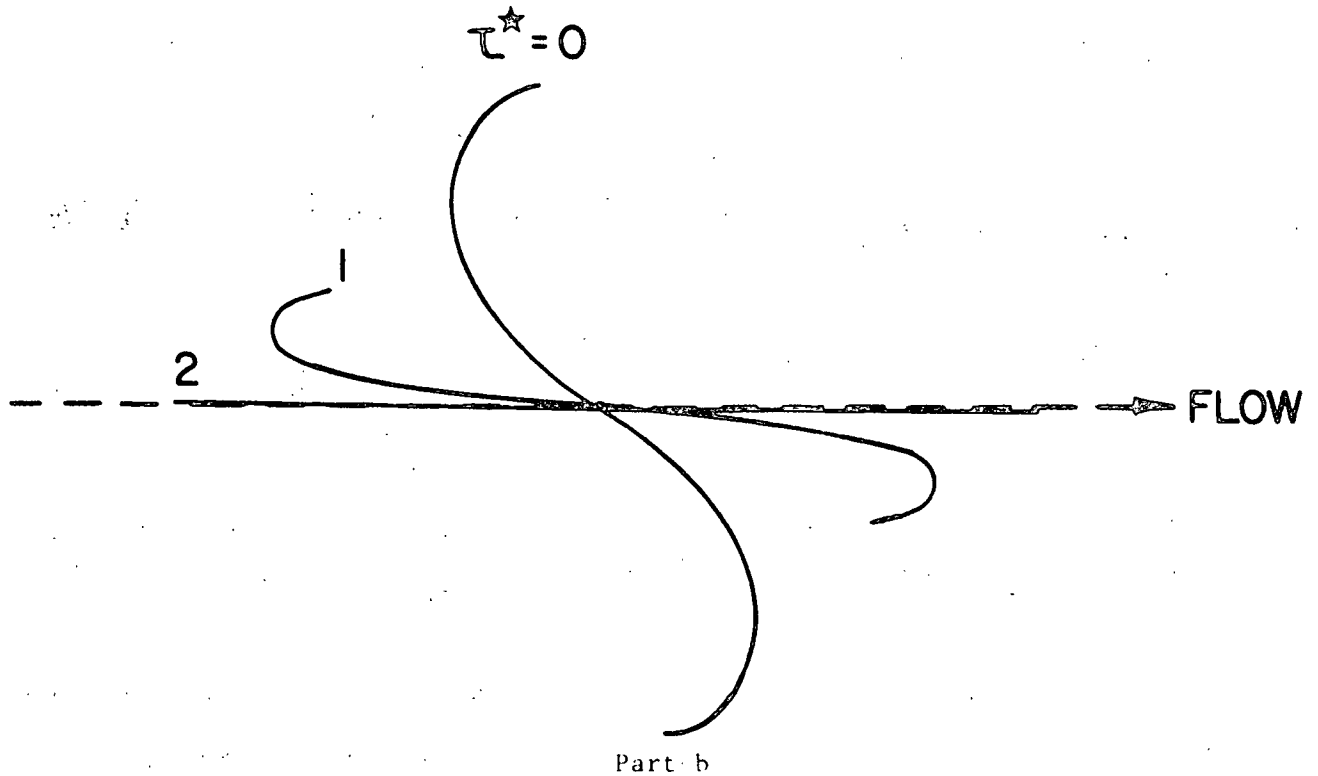

Part b

Figure 25. Evolving shape for initially negatively oriented fiber in simple shear flow (Part a) and simple elongational flow (Part b) using the Goddard-Huang approximation.

the fiber is essentially straight at $\tau^* = 1$ and practically aligned with the flow at $\tau^* = 2$. The effect of the shear flow on the negatively distorted fiber in Fig. 27 results in it rotating and straightening simultaneously. At $\tau = 5$ the straight fiber has about a 15° orientation with respect to the horizontal flow direction.

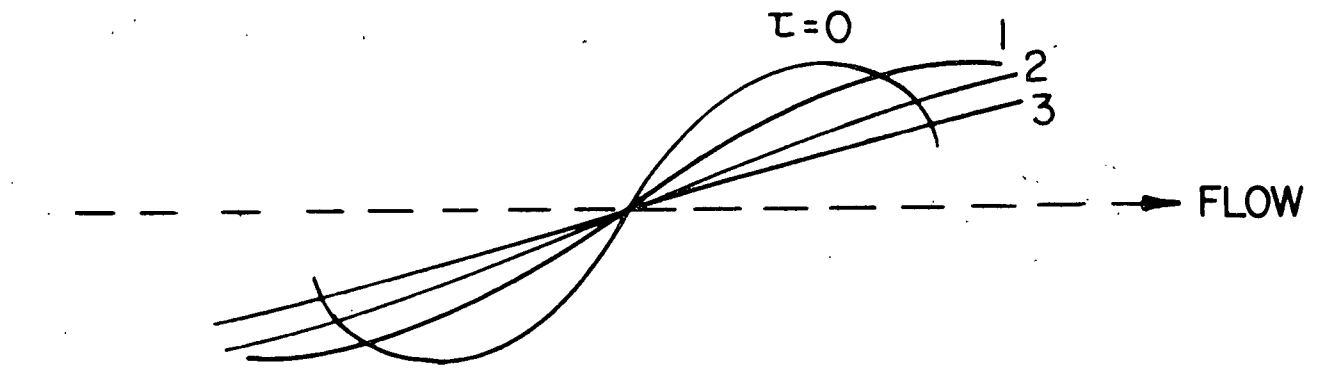

Part a

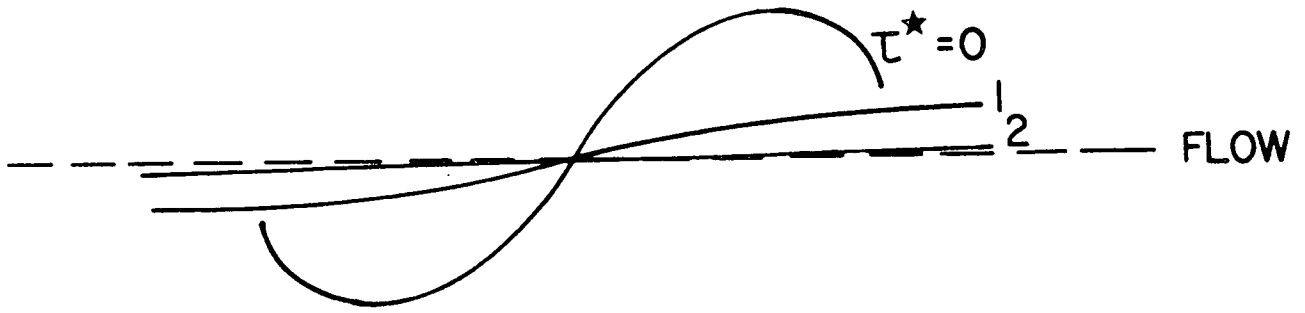

Part b

Figure 26. Evolving shape for initially positively oriented fiber close to horizontal flow direction in simple shear flow (Part a) and simple elongational flow (Part b) using the Goddard-Huang approximation.

These results indicate that the time required to align a fiber in a simple elongational flow is of the order $\tau^* = 2$ and is practically independent of its initial shape and orientation. It is evident from Fig. 24, Part c, and Fig. 25, Part b, that first the fiber is aligned and then straightened by the two-dimensional flow. The

tumbling motion experienced by a fiber in the one-dimensional simple shear flow causes the required time for its alignment to be highly dependent on the initial shape. Parts a and b in Fig. 24 and Part a in Fig. 25 through 27 show that the shear flow tends to simultaneously straighten and align the fiber.

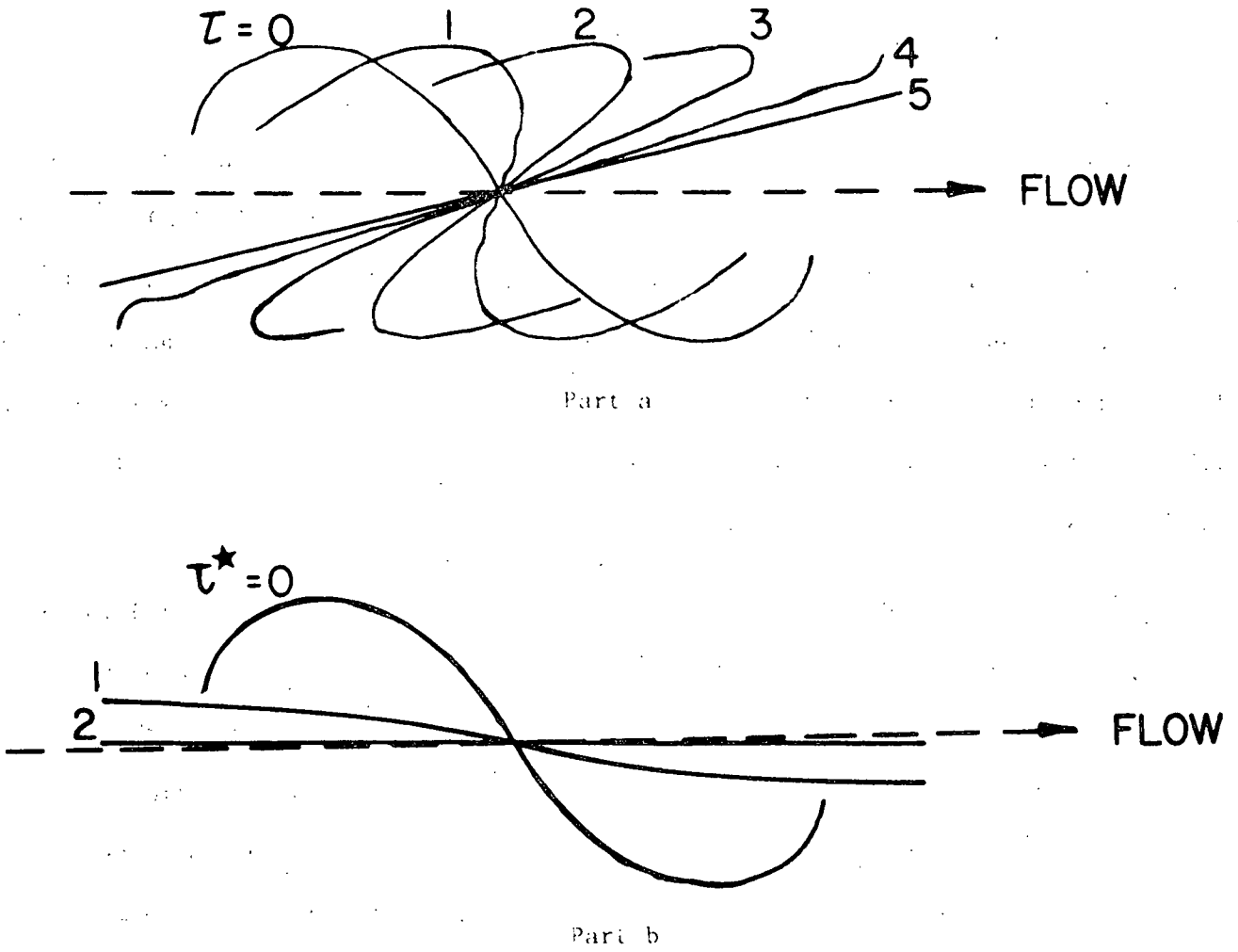

Figure 27. Evolving shape for initially negatively oriented fiber close to horizontal flow direction in simple shear flow (Part a) and simple elongational flow (Part b) using Goddard-Huang approximation.

In a concentrated suspension, where fibers can be oriented in all directions and have very different shapes, it seems unlikely that these could be aligned in any preferred orientation in a shear flow. The high probability of stochastic

fiber-fiber interactions arising as the fibers straighten and align in this flow field could eliminate the possibility of orienting them. Jackson et al. (21) indicate that this is the case in nondilute suspensions of rigid rods undergoing simple shear deformation. The tumbling action being different for fibers with different orientations is primarily responsible for their interaction. When the suspension is subjected to elongational flow, even if they are not completely straightened, the action of aligning the fibers with the flow is the same regardless of their initial shape and orientation, thus, suggesting that aligning fibers in concentrated suspension may only be possible in elongational flows. Harris and Pittman's (22) study of alignment of rigid rods in dilute suspensions using converging flows indicates that the rods align themselves with the direction of flow rather easily. Lee and George (23) concluded that the elongational flow in a converging channel is the most important factor orienting glass fibers suspended in epoxy resins. It is yet to be observed if a similar behavior occurs in concentrated suspensions.

The only fiber shapes in which some warping is evident are at $\tau = 1$ in Part a of Fig. 25 and 27, the effect being more pronounced in the former. The warping occurs near the center of mass of the fiber where the velocity is low and the first term in Eq. (18) representing the motion of the fiber along its axis becomes important. Although the overall features of the evolution of the shape are not lost when using the Goddard-Huang approximation, neglecting the curvature of the fiber leads to different results as shown in Fig. 28. In this figure, at $\tau = 1$, the fiber has points of large curvature which were not evident when it was neglected (Fig. 27). In addition, the time required for the fiber to straighten and its axis to be oriented at 15° from the horizontal is $\tau = 6$ compared to $\tau = 5$ in Fig. 27. Therefore, if the fiber has points of extreme curvature even in a concentrated suspension, the Goddard-Huang approximation is not valid.

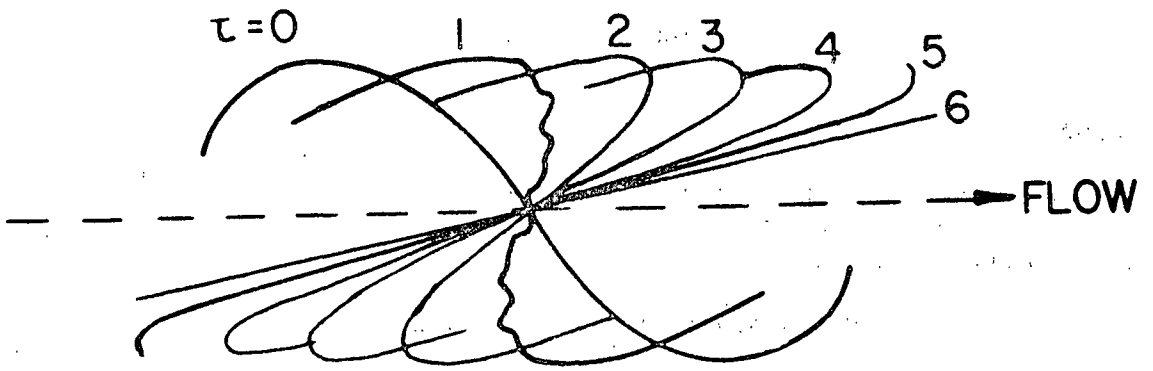

Figure 28. Evolving shape for initially negatively oriented fiber close to horizontal flow direction using Eq. (1) and (2) with K_n/K_s = 0.172.

NOMENCLATURE

a	radius of fiber
C	fiber concentration (% by wt.)
C_v	fiber volume concentration
C^{12}	mean square value of intermittent reflected light
F	probability distribution representing orientation of neighboring fibers per unit length along s
f	frequency
G_x	power spectral density function of signal x(t)
G_{xy}	cross-spectral density function of signals x(t) and y(t)
$\underset{\approx}{I}$	unit tensor
$\underset{\approx}{K}$	fiber mobility tensor
K_s	longitudinal component of $\underset{\approx}{K}$
K_n	normal component of $\underset{\approx}{K}$
k	curvature of fiber $(= \left\| \partial^2 \underset{\sim}{x} / \partial s^2 \right\|)$
$\underset{\approx}{L}$	velocity-gradient tensor
ℓ	wavelength in PSD and coherence analyses; half arc-length of fiber in fiber straightening and alignment analysis
N	number of neighboring fibers per unit length along s
p'^2	mean square value of pressure fluctuations
PSD	power spectral density function
$\underset{\approx}{R}$	hydrodynamic resistance tensor to fiber mobility
$\underset{\approx}{R}'$	hydrodynamic resistance tensor between two adjacent fibers
RPSD	power spectral density function
s	position along arc-length of fiber
Δs	increment in s
t	time

Δt	increment in t
$\underset{\sim}{x}$	position vector along axis of fiber
x(t), y(t)	random signals

Greek Symbols

α	length-to-diameter aspect ratio of fiber
γ_E	elongational rate
γ_{s_2}	shear rate
γ_{xy}	coherence function between x(t) and y(t)
$\underset{\sim}{\delta}$	unit vector normal to fiber's axis ($= \frac{1}{k} \partial^2 \underset{\sim}{x} / \partial s^2$)
ε	dimensionless fiber-fiber separation
θ	angular position along fiber's circumference
μ	viscosity of suspending medium
τ	dimensionless shear time
τ^*	dimensionless elongational time
ψ	angle with respect to fiber's axis

LITERATURE CITED

1. Mason, S. G. The flocculation of cellulose fiber suspensions. Pulp Paper Mag. Can. 49:99-104(1948).

2. Meyer, E. G. Feasibility of high consistency forming. Tappi 59(3):56-57(1976).

3. Wahren, D. Fiber network atructures in papermaking operations. Proc. Conf. Paper Science and Technology - The Cutting Edge. The Institute of Paper Chemistry, Appleton, WI, May 8-10, 1979. p. 112-129.

4. Grundström, K.-J., Norman, B., and Wahren, D. High-consistency forming of paper. Tappi 56:81-84(1973).

5. Grundström, K.-J., Meinander, P. O., Norman, B., Reiner, L., and Waris, T. High-consistency former. Tappi 59(3):58-61(1976).

6. Kerekes, R. J. and Garner, R. G. Measurement of turbulence in pulp suspensions by laser anemometry. Transactions CPPA 83:TR53-60(1982).

7. Giebner, H. R. The response of higher consistency fiber suspension to shear forces. M.S. Report, The Institute of Paper Chemistry, Appleton, WI, 1982.

8. Goddard, J. D., Huang, Y.-H., and Huang, L.-C. Rational prediction of composite properties based on asymptotic micromechanics. Proc. 9th U.S. Congress on Applied Mechanics, 1982:197-211.

9. Kerekes, R. J. and Garner, R. G. Measurement of turbulence in pulp suspensions by laser anemometry. Transactions CPPA 83:TR53-60(1983).

10. Appel, D. W. Measurements of flocculation in flows of fiber suspensions through nozzles. Proc. 26th TAPPI Engineering Conf., 1971:345-360.

11. Nerelius, L., Norman, B., and Wahren, D. Measurement of flocculation characteristics by light reflection. Tappi 55:574-80(1972).

12. Abed, R. The characterization of fluidized nonuniformity in large fluidized beds. Paper 80a, AIChE 1982 Annual Meeting, Los Angeles, CA, Nov. 14-19, 1982.

13. Tsuji, Y. and Morikawa, Y. Flow pattern and pressure fluctuation in air-solid two-phase flow in a pipe at low air velocities. Int. J. Multiphase Flow 8:329-41(1982).

14. Duffy, G. G. and Norman, B. G. Fiber flocculation in conical contractions simulating the paper machine flowbox slice. Proc. Int. Symp. on Paper Machine Headboxes, McGuill Univ. 1979:43-53.

15. Bendat, J. S. and Piersol, A. G. Random data: analysis and measurement procedures, J. Wiley & Sons 1971:31-4.

16. Hinch, E. J. The distortion of a flexible inextensible thread in a shearing flow. J. Fluid Mech. 74:317-33(1976).

17. Goddard, J. D. and Huang, Y.-H. On the motion of flexible threads in a stokes shear field. J. Non-Newt. Fluid Mech. 13:47-62(1983).

18. Doi, M. and Edwards, S. F. Dynamics of concentrated polymer systems, Part 1. Brownian motion in the equilibrium state. J. Chem. Soc. Faraday Trans. II, 74:1789-1801(1978).

19. Doi, M. and Edwards, S. F. Dynamics of concentrated suspensions, Part 4 - rheological properties. J. Chem. Soc. Faraday Trans. II, 75:38-54(1979).

20. Finlayson, B. A. Nonlinear analysis in chemical engineering. McGraw-Hill Book Co. 1980:113-26.

21. Jackson, W. C., Folgar, F., and Tucker, C. O. Prediction and control of fiber orientation in molded parts. Paper 7c, AIChE Annual Meeting, Los Angeles, CA, Nov. 14-19, 1982.

22. Harris, J. B. and Pittman, J. F. T. Alignment of slender rod-like particles in suspension using converging flow. Trans. Inst. Chem. Engrs. 54:73-83(1976).

23. Lee, W.-K. and George, H. H. Flow visualization of fiber suspensions. Polymer Eng. Sci. 18:146-56(1978).

THE INSTITUTE OF PAPER CHEMISTRY

Evaristo J. Bonano

*Evaristo J. Bonano

Clyde H. Sprague

Clyde H. Sprague
Director
Engineering Division

*Now with: Sandia National Laboratories, Albuquerque, New Mexico 87185